**Hannes N.
Radenbach**

**Emissão radiativa de nanopartículos de
Gd2O3:Er/Yb excitadas no infravermelho próximo**

**Radiative Behaviour of Gd2O3:Er/Yb nanoparticles
under near infrared illumination**

Tese apresentada à Universidade de Aveiro para cumprimento
dos requisitos necessários à obtenção do grau de Mestre em
ciência e engenharia de materiais, realizada sob a orientação
científica do Professor Catedrático Luís António Ferreira Martins Dias Carlos, Professor do Departamento de Física da Universidade de Aveiro

o júri / the jury

presidente / president

Ana Margarida Madeira Viegas de Barros Timmons
Professor auxiliar, Departemento de Química, Universidade de Aveiro

vogais / examiners committee

Nuno João Silva
Investigador auxiliar, Departemento de Física, Universidade de Aveiro

Luís António Ferreira Martins Dias Carlos
Professor Catedrático, Departemento de Física, Universidade de Aveiro

Acknowledgements

Many thanks to all the people that supported me during my thesis. First of all, there is Dr. Mengistie Leweyehu Debasu, post-doc fellowship holder at CICECO and the departments of Physics and Chemistry at the University of Aveiro, who helped me actively during most my experiments and engaged in fruitful discussion about the interpretation of my results; lastly, he supplied me with some results of his own. Secondly, I want to thank Luís António Ferreira Martins Dias Carlos, full professor at the Physics department of the University of Aveiro, for providing me with the research topic of my thesis and helping me with the interpretation of my results. Then, there are all the people that made the everyday life in the labs even more interesting, like Cynthia, Tom and Sangeetha and Carlos.

Even more, I want to thank my friends that made my stay in Portugal a memorable and awesome experience. First of all to my flatmate Manon, and to Louise, Antoine, Juju, Tania, Sven, Thekla, Torben, and Lena-Lotta. Thank you for sharing with me all these experiences in the portuguese cities and their cute little cafés; in, on or next to rivers, and in beautiful nature of the back country of Portugal.

Also, I am thankful towards the FAME Master Program that granted me with the great opportunity to study abroad during two years and supported me with a scholarship and also personally. Here I want to thank especially Eirini Sarigiannidou from the INP Grenoble and Ana Barros from the University of Aveiro, but also all the others involved in the program.

My greatest gratitude goes to my parents for always supporting me in what I wanted to do and enabling me to live abroad for two years. Finally, this thesis would not have been possible without the not only moral support from my amazing girlfriend Achsah Venter, who helped me through times of frustration and made me see many things in a different light.

Thank you so much!

Resumo

Nanopartículas mostrando conversão ascendente de energia têm atraído recentemente muita atenção, sobretudo tendo em vista aplicações médicas e biológicas, tais como o mapeamento in vivo da temperatura intercelular ou o desenvolvimento de técnicas de diagnóstico de doenças cancerosas. O sistema estudado anteriormente de nanobastões de óxido de gadolínio co-dopados com érbio e itérbio e decorados com nanopartículas de ouro mostrou potencialidades como nanotermómetro eficaz numa gama de temperatura desde os 300 até aos 2000 K. Neste trabalho, um estudo mais detalhado do comportamento morfológico e radiativo destas partículas foi realizado. Verificou-se que o limiar de potência de laser para o início da radiação de corpo negro diminui fortemente com o aumento da concentração de ouro. A temperatura correspondente ao limiar do processo de emissão de corpo negro parece manter-se aproximadamente constante, independentemente da concentração de ouro à superfície dos nanobastões. A eficiência de aquecimento foi determinada, tendo-se mostrado que ela aumenta significativamente com a concentração de ouro. A análise morfológica aos nanobastões revelou que a temperatura no limiar da radiação do corpo negro não é suficiente para induzir transformação significativas nem os nanobastões nem nas nanopartículas de ouro, como era de esperar partir da comparação com a literatura. No entanto, foram detetadas alterações significativas nas propriedades radiativas e na morfologia dos nanobastões decorados com a s nanopartículas de ouro que foram submetidos a forte aquecimento induzido pela excitação laser.

Abstract

Upconverting nanoparticles have attracted much attention in science recently, specifically in view of medical and biological applications such as live imaging of cell temperatures or cancer treatment. The previously studied system of gadolinium oxide nanorods co-doped with erbium and ytterbium and decorated with different number densities of gold nanoparticles has been studied. So far, these particles have been proven as efficient nanothermometers in a temperature range from 300 up to 2000 K. In this work, a more detailed study on the morphological and radiative behaviour of these particles has been conducted. It was found that the laser power threshold for the onset of the black body radiation decreases strongly with the increase in the gold concentration. The temperature of the onset itself seems to remain approximately constant. The heating efficiency was determined to increase significantly with the gold concentration. The morphological study revealed that the temperature at the black body radiation threshold was not enough to induce any significant transformation in neither the nanorods nor the gold nanoparticles, as was expected from comparison with literature. However, significant changes in radiative properties and the morphology were detected for powders that underwent strong laser heating until the emission of brightly visible black body radiation.

CONTENTS

LIST OF FIGURES

LIST OF TABLES

THEORETICAL BACKGROUND

1.1 UPCONVERSION LUMINESCENCE IN RARE EARTH IONS

1.1.1 *Relevance of Rare Earth Ions*

Contrarily to what their group name might indicate, rare earth elements are not actually rare in the meaning of a small abundance. In fact, only one element, promethium, is very rare due to its radioactive nature with a short decay time (2.6 years for the most stable isotope [1]). Even the most rare of the stable rare earth elements, thulium, is still more abundant than gold or platinum [2]. The name 'rare earth' originates from the beginning of their discovery. In the 18th century, rare earth elements were only available in the form of their oxides that were produced from rare minerals, thus the name [3, 4]. The first rare earth elements were found 1787 near Ytterby, Sweden, which gave its name to several of the elements such as ytterbium, yttrium, terbium and erbium.

Rare earth atoms exhibit interesting optical properties in their divalent and trivalent ionic states. In this work, only the trivalent ions shall be covered, the term 'ion' is therefore equal to 'trivalent ion'. In this state, all optical emission and absorption features originate from transitions of the electrons in the partially filled 4f shell. These intra-4f transitions are of particular interest because despite the fact that the 4f-shells are the energetically highest shell of the rare earth ions, they spatially lie 'within' the 6s and 5d shells, as can be seen by the electronic density distribution in Figure 1.1.
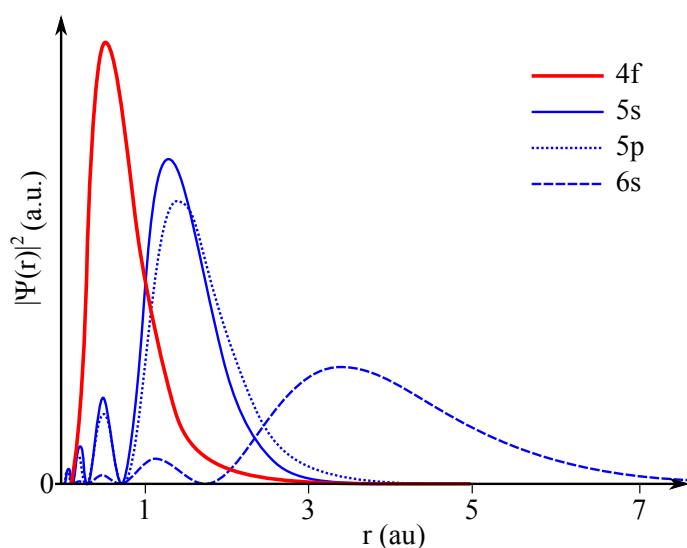

Figure 1.1: Probability density distribution for electrons in different shells as a function of the distance from the nucleus. The diagram represents Gd^+ but is qualitatively valid for the other rare earths as well. Redrawn from [1].

Because of this shielding, the RE chemistry is mostly dependent on the behaviour of the outer 6s and 5d electrons. The resulting similar chemical behaviour made it so difficult to obtain highly pure RE samples in the beginning of their research.

Secondly, as the 4f electrons have almost no contribution to the chemical state of the ion, the respective energy levels remain virtually unchanged. Energy of states only change between a few (for low-lying states) and a few hundred (for high energy states) wavenumbers in different environments (see, *e.g.,* Dieke [1] or Table 1.1). Additionally to the low sensitivity to the host, the host-induced energy-splitting of the single levels is only very weak. Because of the weak interaction with the lattice, the energy levels have little to no vibronic structure. The poor ion-host interaction allows for long excited-state lifetimes. The non-radiative decay mechanisms are very inefficient, leading to lifetimes in the millisecond range [5–7].

1.1.2   *Photon Induced Upconversion Using the Erbium/Ytterbium System as Example*

Upconverting materials are capable of emitting photons with a shorter wavelength than the wavelength of the exciting light. In order to not violate the law of energy conservation, they therefore absorb several photons for the emission of a single one. Thus, they rely on intermediate metastable states that can be occupied after the absorption of a first photon. To achieve reasonable upconversion efficiencies, these intermediate states need certain lifetimes in order to allow anew excitation to take place on an already excited centre. Erbium excited states possess lifetimes of several hundred microseconds [8] which is enough to make them a good candidate for upconversion applications.
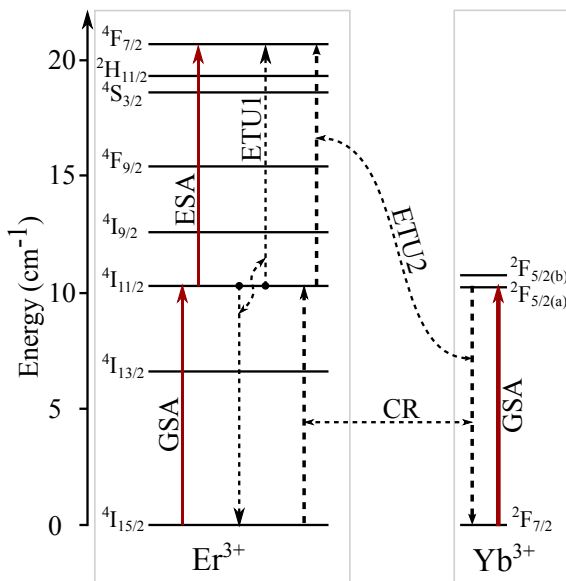
Figure 1.2: Energy level diagram of the system erbium/ytterbium depicting the upconversion paths. The different excitation and energy transfer mechanisms are labelled respectively: ground state absorption (GSA), cross relaxation (CR), excitet state absorption (ESA) and energy transfer upconversion (ETU1, ETU2).

To understand the upconversion process, we consider the system Er/Yb whose energy levels are shown in Figure 1.2. The ytterbium ion only possesses two energy levels above the ground state which can be excited with a 980 nm light source. Erbium possesses a more complicated energy level diagram. At first, we shall only consider the energy levels $^4I_{15/2}$, $^4I_{11/2}$ and $^4F_{7/2}$ which are approximately equidistant in energy with a spacing that corresponds to a 980 nm photon (*cf.* data in Table 1.1).

Upon illumination with a 980 nm light source, erbium can be excited to $^4I_{11/2}$ in two ways,

either directly by ground state absorption (GSA) of one photon, or ytterbium absorbs a photon and subsequently transfers its energy to the erbium ion, *via* cross relaxation (CR). The now excited erbium ions can proceed in two different ways, it can either relax back to its ground state or absorb another quantum of energy. This can happen either directly by excited state absorption (ESA) or by energy transfer from an excited ytterbium or erbium ion which is called energy transfer upconversion (ETU1 and ETU2 in Figure 1.2). Hewes and Sarver have shown that for the ytterbium concentrations used in this work, both excitations are very likely to take place by energy transfer from the ytterbium instead of a direct ground/excited state absorption [9].

The erbium ion is now in the $^4F_{7/2}$ state and can emit a photon in the green range, which has a higher energy than a single photon from the excitation source. In reality it will quickly undergo a non-radiative relaxation to the more stable thermally coupled states $^2H_{11/2}$ and $^4S_{3/2}$, and emit from these states. This is depicted in Figure 1.3 around 540 nm.
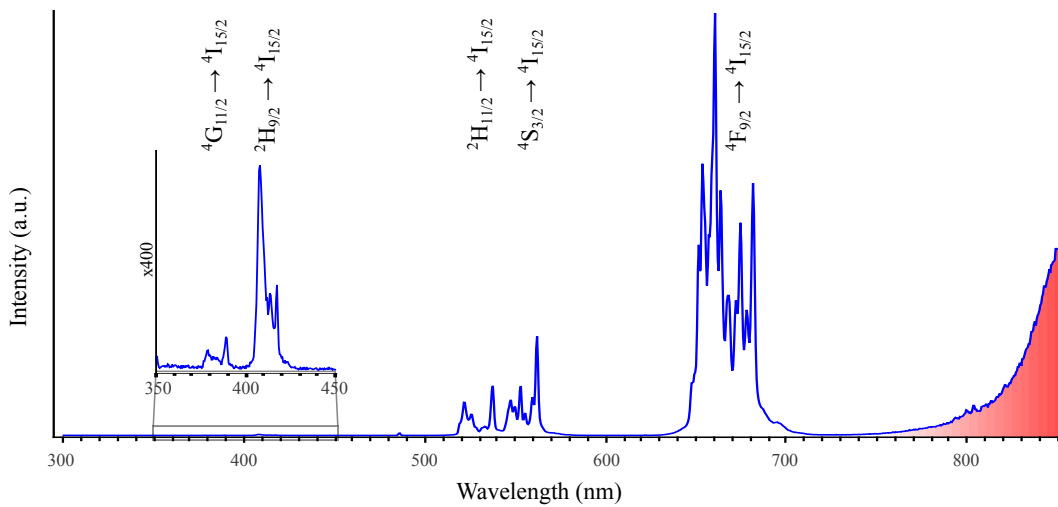
Figure 1.3: Erbium emission spectrum in erbium/ytterbium co-doped Gd_2O_3 nanorods. The electronic transitions responsible for each emission are labelled respectively. Note the magnification of the inset. The part above 750 nm shaded in red is a laser effect that is disconnected from the erbium emission.

In reality, the above way is not the only upconversion pathway that is followed. As can be seen, the spectrum also exhibits emission in the ultraviolet and blue around 380 and 407 nm, and the red around 660 nm. After the first excitation, a non-radiative relaxation to $^4I_{13/2}$ followed by the absorption of another energy quantum leads to the emission from $^4F_{9/2}$ [10] in the red region. On the other hand, the upconversion described above does not need to stop at the $^4F_{7/2}$ level and can lead to emission from even higher energy levels such as $^4G_{11/2}$ and $^2H_{9/2}$ or in the ultraviolet and blue region [10, 11].

The presence of the ytterbium is not necessary to allow for upconversion in the erbium ion, but it strongly enhances the efficiency. Ytterbium has a ten times larger absorption cross-section [4, 12, 13] for near infrared light compared to erbium, and energy transfer from ytterbium to erbium is efficient [14]. The ytterbium acts as a sensitizer, the erbium is called an activator.

Upconversion emission intensities are influenced by further factors such as the concentration of either ion, the pump power used for excitation and the highest phonon energy. Decreasing

the concentration of the ions increases their centre-to-centre distance and renders the energy transfer between ytterbium and erbium more unlikely. Varying the pump powers also varies the relative populations in the different energy levels because of the non-linear dependency of some transition rates and thus non-linearly changes the emission intensity as a function of the pump power. This can also be used to identify the mechanism responsible for the excitation. Non-radiative relaxation is more efficient when fewer phonons have to be involved, thus materials with lower highest phonon energies will have a lower contribution of non-radiative relaxation.

Electronic configuration	Energy (cm^{-1})		
Er^{3+}			
	Host:		
	Free Ion	GdCl$_3$	Y$_2$O$_3$
$^4I_{15/2}$	0	0	0
$^4I_{13/2}$	6 485.9	6 479.31	6 458.2
$^4I_{11/2}$	10 123.6	10 107.23	10 073.3
$^4I_{9/2}$	12 345.5		12 287.9
$^4F_{9/2}$	15 182.85		15 071.1
$^4S_{3/2}$	18 299.6		18 072.0
$^4H_{11/2}$	19 010.8	19 014.53	18 931.3
$^4F_{7/2}$	20 494.1		20 267.5

	Yb^{3+}	
	Host:	
	Ethyl Sulfate (77 K)	YAG (4.2 K)
$^2F_{7/2}$	0	0
$^2F_{5/2}$	10 260.6	10 324.6

Table 1.1: Russel-Saunders term symbols and respective mean energies for the lower electronic configurations of Er^{3+} and Yb^{3+}. Different hosts were chosen to point out the host effects. Crystal field splitting is neglected in that only the mean value for each energy level is given. All values taken from Dieke [1].

Despite being one of the central quantities in thermodynamics, statistical mechanics and our everyday world, temperature is not directly observable. It has no operator representation in quantum mechanics [15]. Thus it is defined in different ways. Thermodynamics state that two systems that can exchange energy and are in a thermal equilibrium have the same temperature. Here, temperature can only be determined by a reference. Often, the ideal gas law is used:

$$T = \frac{pV}{nR},$$
(1.1)

where p is the pressure, V the volume and n the number of atoms in mol in the sample. R is the gas constant. If these three quantities are known, the temperature is known as well. Statistical mechanics, on the other hand, define temperature as the derivative of the internal energy E with respect to the entropy S at constant volume and number of particles:

$$T = \left(\frac{\partial E}{\partial S} \right)_{N,V}$$
(1.2)

Temperature can not be measured directly, thus thermometry today relies on measuring the change of certain properties of a material and correlate the change with the change in temperature. Until now, researchers all around the world have come up with various kinds of nanothermometry methods. They are based on a large variety of different effects, yet they are all based upon the above principle. The thermometry methods used in this work make use of the luminescence from nanoparticles under laser illumination, namely the upconverted green light emission from erbium ions induced by the laser illumination directly (*cf.* Section 1.2.1) and the black body radiation induced by the strong heating of the particles under illumination (*cf.* Section 1.2.2).

1.2.1   *Sensing Based on Fluorescence Intensity Ratio*

1.2.1.1   *Luminescence Intensity from a Single Level*

The intensity of a transition from an excited level to a lower level, often the ground state, is in general temperature dependent. This is due to the nature of the quenching which is phonon-driven. Non-radiative decay becomes highly inefficient when more then five (sometimes four) phonons are needed to span the energy gap between two adjacent levels [16]. Thus, the rate constant for the quenching of a single excited level is strongly temperature dependent [17] because the highest phonon energy changes with temperature.
The intensity evolution with temperature for the emission from a level at the energy E above the ground state at a constant excitation power can be given by [18]

$$I \propto gA\omega \exp\left(-\frac{E}{kT} \right)$$
(1.3)

with g, A, ω the degeneracy, the spontaneous emission rate and the angular frequency of the emission, and k and T the Boltzmann constant and absolute temperature.

1.2.1.2   *Luminescence from Thermally Coupled Levels*

Many systems, such as rare earth ions, possess several energy levels that can be occupied by exciting the respective luminescence centre with a certain amount of energy. Some of the energy levels, additionally, are only separated by a small amount of energy ΔE from one or more neighbouring levels. In this case, small refers to an energy in the same order of magnitude as the thermal energy of the system at the desired working temperature. In this case, occupying the lower of the two levels by, *e.g.*, photon absorption will lead to the thermal redistribution of occupied levels between the lower, directly excited level, and the upper neighbour (*cf.* Figure 1.4). The respective ratios are fixed and given by a Boltzmann distribution [5]:

$$\frac{N_2}{N_1} = \exp\left(-\frac{\Delta E}{kT}\right) \tag{1.4}$$

where N_2, N_1 are the upper and lower level's population, respectively. The intensity of a certain radiative transition is directly proportional to the occupation of the emitting level. In turn, FIR is defined as the ratio of the emission intensities. This yields:

$$\text{FIR} = \frac{I_2}{I_1} = \frac{N_2}{N_1} = \frac{g_2 A_2 \omega_2}{g_1 A_1 \omega_1} \exp\left(-\frac{\Delta E}{kT}\right) = B \exp\left(-\frac{\Delta E}{kT}\right) \tag{1.5}$$

Here, I_i are the emission intensities from level i to the ground state and ΔE is the energy splitting between the two levels. It is apparent that FIR changes drastically with temperature when the thermal energy of the system is of the same order of magnitude as the energy level splitting ΔE (*cf.* Section A.3). The comparison of two levels makes the absolute intensities negligible and thus avoids the excitation power dependency. The parameter B can be determined by extrapolation of the FIR curve in an Arrhenius plot.
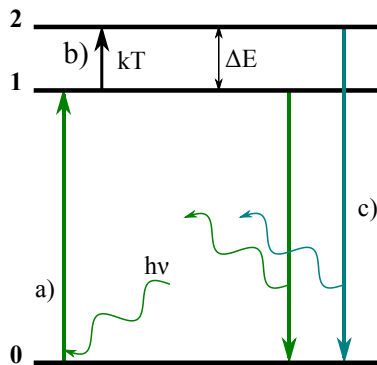
Figure 1.4: Schematic of a three level system where the excited levels 1 and 2 are separated by an energy gap ΔE in the same range as the thermal energy of the system. a) Excitation of the system with photons leads to the population of level 1. b) Thermal energy is enough to promote ions from level 1 to level 2, until a steady state with the population ratio given by (1.4) is reached. c) Excited states also emit photons when relaxing back to the ground state, the wavelength of the emission is different for the different excited states.

All luminescent materials that have two states with a sufficiently small energy separation can in theory be used for temperature sensing. However, to be able to apply (1.5), those states must be coupled only by thermal redistribution. E.g., it has been shown that for Eu^{3+} the redistribution of population between the levels depends more on the energy transfer rate between ions than on the thermal coupling of the levels [19]. Therefore, FIR does not obey (1.5).

A few general rules apply for the energy splitting of the two coupled levels [7]:

- The energy gap should be larger than ≈ 200 cm^{-1} (25 meV) to avoid any significant overlap between the coupled emissions

- The energy gap should be below 2000 cm^{-1} to obtain a reasonable luminescence intensity from the upper level
- Both coupled levels should lie at least 3000 cm^{-1} above the next lower level to avoid non-radiative transitions and increase the luminescence yield

Many of the rare earth ions fulfil these requirements, explaining their extensive use for temperature sensing. In erbium ions, $^4S_{3/2}$ and $^2H_{11/2}$ are commonly used for temperature sensing with the FIR method. The energy gap between the levels is reported to be around 700 to 800 cm^{-1} [20, 21]. The next lower state is seperated by approximately 3000 cm^{-1} (*cf.* Table 1.1), erbium thus complies very well to the general rules above very well. Values of B for erbium thermometers usually lie within $1.5 \leq B \leq 3.2$ [12, 20].

Yet, rare earth ions are by far not the only luminescent species used. Other systems include coupling between a rare earth level and an energetically close host level [22], levels within the organic dye Rhodamine B [23] or transition metal-doped quantum dots [24].

1.2.2   *Sensing Based on Black Body Radiation*

The effect of black body radiation is already long known. As an example, blacksmiths could easily determine the approximate temperature of their forging metals by the colour of their glow. This was possible since the colour of the emission depends on the temperature of the matter. Scientific treatment of the effect began in the middle of the 18th century. It was known that hot bodies emitted a continuous spectrum that only depended on the temperature of the body, not on its material. This radiation was called black body radiation. The so-called black body was defined as an ideal body that absorbs all incident radiation and is at equilibrium with the radiation of its surroundings. In this steady state, a black body emits radiation with a spectrum characteristic of only its temperature. This spectrum tends towards zero for very high and very low frequencies and possesses a maximum in between. In 1894, Wien formulated his displacement law, stating that the wavelength of the maximum, λ_{max}, and the corresponding temperature of the body, T, obey to the law

$$\lambda_{max} \cdot T = const. \tag{1.6}$$

Lord Rayleigh derived an equation to describe the spectrum itself as a function of temperature. However, even though it is accurate for small frequencies, it does not reach a maximum; the predicted energy emission by a black body therefore is infinite for any temperature. Max Planck solved this problem with the assumption that atoms can only possess an integer multiple of a minimal energy unit

$$\epsilon_n = nh\nu \tag{1.7}$$

whose energy depends on the frequency ν. n is an integer and h is the newly-introduced Planck quantum. Planck associated a mean energy to the oscillators of a system:

$$\bar{\epsilon} = \sum_{n=0}^{\infty} p_n \epsilon_n \tag{1.8}$$

where p_n is the probability of an oscillator being in a state n and is given by

$$p_n = \frac{e^{-\frac{\epsilon_n}{kT}}}{\sum_{n=0}^{\infty} e^{-\frac{\epsilon_n}{kT}}}. \tag{1.9}$$

Some straightforward calculus leads to an easier expression for the mean energy:

$$\bar{\epsilon} = h\nu \frac{\exp\left(-\frac{h\nu}{kT}\right)}{1 - \exp\left(-\frac{h\nu}{kT}\right)} \tag{1.10}$$

The solution of the wave equation yields for the density of vibrational states, assuming the wave function needs to be zero on the walls of the body:

$$dN_\nu = \frac{8\pi}{c^3}\nu^2 d\nu \tag{1.11}$$

and with $dU = \bar{\epsilon}dN_\nu$:

$$dU = \frac{8\pi h\nu^3}{c^3}\frac{\exp\left(-\frac{h\nu}{kT}\right)}{1 - \exp\left(-\frac{h\nu}{kT}\right)}d\nu = \rho(\nu)d\nu \tag{1.12}$$

where $\rho(\nu)$ is the energy density at a certain frequency. ρ can also be expressed as a function of wavelength, yielding

$$\rho(\lambda) = \frac{8\pi hc}{\lambda^5}\frac{\exp\left(-\frac{hc}{\lambda kT}\right)}{1 - \exp\left(-\frac{hc}{\lambda kT}\right)}. \tag{1.13}$$

Wien's displacement law can be derived from (1.13) by setting the first derivative to zero, which leads to

$$\lambda_{max}T = \frac{hc}{5k}. \tag{1.14}$$

For known combinations of λ_{max} and T, h has been calculated to be $h \approx 6.7 \cdot 10^{-34}$ Js which is not far from its real value of $h = 6.626 \cdot 10^{-34}$ Js.
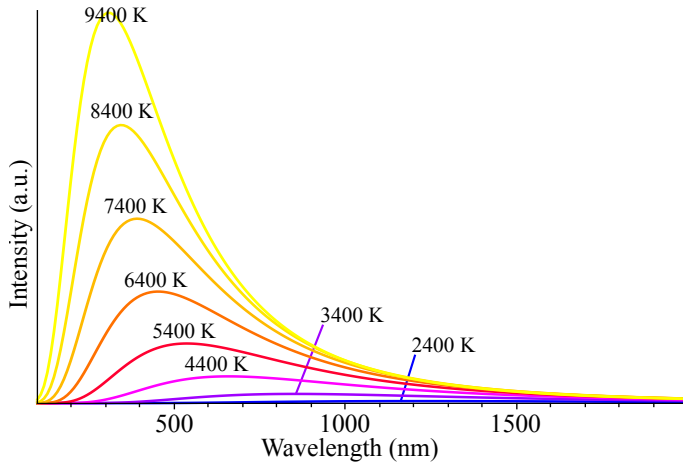
Figure 1.5: Ideal emission spectra of a black body at different temperatures using (1.13). The blue-shift of the maximum with higher temperatures is evident.

Temperature measurements through black body radiation can be either done by: determining the maximum of the energy density distribution, given the full spectrum has been acquired, or otherwise, (1.13) can be used for fitting, yielding the absolute temperature of the sample. This method has the advantage that it is completely non-invasive compared to the FIR method, where the incident radiation needed for excitation can alter the sample temperature. It is capable of resolving a sample's temperature temporally down to tens of mi-

croseconds and thermally down to a tenth of a Kelvin. On the other hand, spatial resolution is limited by the Rayleigh limit and usually does not surpass 10 μm [18].

1.2.3   *Limitations of Nanothermometers*

When decreasing the size of thermometers, problems will arise that do not exist for macroscopic thermometers and that are mostly related to quantum mechanics. *E.g.,* shot noise or tunnel junction conduction can arise in thermoelectric thermometers [5]. These might be problems that arise from electronic conduction on the nanoscale, nevertheless luminescent thermometers suffer from nanoscale problems as well.

First of all, the general existence of local temperature in dependence of the size of a sample has been challenged [15, 25]. Hartmann developed a model [25], applied it to silicon and found some surprising results (*cf.* Figure 1.6). Hartmann obtained his result from the assumption of a linear chain and neglecting other processes such as phonon scattering. The minimum length scale for the existence of the local temperature is quite high, in the order of 100 nm.
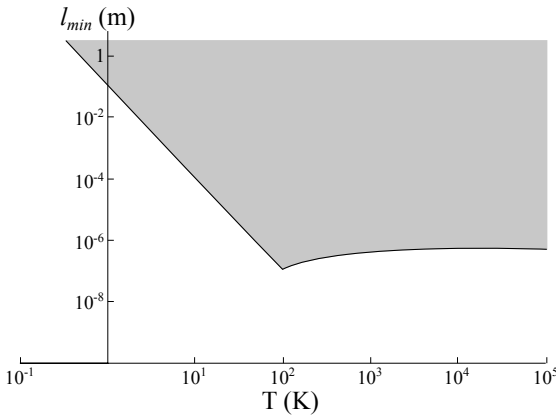
Figure 1.6: Minimum length of a linear chain of silicon atoms for the existence of local temperature. In the area shaded in grey, local temperature exists according to the model of Hartmann. Redrawn from [15].

Assuming that the concept of a local temperature is valid in the particles used for thermometry, another factor has to be considered which is the accuracy of the thermometer. Alicki and Leitner developped a model to estimate the maximum accuracy a thermometer can have as a function of its size [26]. The result of their calculations is:

$$\frac{\delta T}{T} = \left[\frac{4T}{3\sqrt{3}T_D} \exp\left(\frac{3T_D}{8T} \right) \right] \frac{1}{\sqrt{N_A}}, \tag{1.15}$$

where δT is the accuracy in K, T, T_D is the absolute and the Debye temperature of the particle, respectively, and N_A is the number of atoms in the thermometer particle. The term in square brackets for T = 300 K is usually around 1 (1.27 for diamond, T_D = 1860 K; 0.87 for T_D = 100 K), therefore (1.15) can be simplified to

$$\delta T = \frac{T}{\sqrt{N_A}}. \tag{1.16}$$

The accuracy of nanothermometers therefore decreases with decreasing size.

The above points demonstrate new problems when discussing thermometry on the nanoscale. The result from Hartmann has to be treated carefully as his model is exact, but not its application to material. Yet, it is interesting to see that there is a lower limit below which it is useless to define the concept of local temperature and that it must be kept in mind when

discussing thermometry at very small scales. The maximum theoretical accuracy is important to know as for nanoparticles δT can take quite large values that get into the range of the measurement accuracy and have to be considered when discussing thermometer accuracies or considering thermometer sizes in the 1 nm-range.

1.3   OPTICAL HEATING WITH GOLD NANOPARTICLES

The particles used in this work were made up of two main parts: the doped nanorods and the attached gold nanoparticles. While the task of the rods is mainly to create the upconversion luminescence for temperature sensing at low temperatures and to support the gold nanoparticles, the latter serve for efficient heating. The ability of highly efficient and localised heating through the absorption of light has attracted much attention to noble metal nanoparticles in general. They are currently used in enhancing imaging techniques or allow for single molecule detection [27] and their use in biological and medical field for *e.g.* drug delivery is under current research [28]. Advances in chemical synthesis have made it possible to produce particles in a variety of even exotic shapes like stars and of different sizes down to only a few nanometers [29–32].

Most research is done with interest to their surface plasmonic properties. Surface plasmons are collective charge oscillations that occur at the interface between conductors and dielectrics. They can take various forms, ranging from freely propagating electron density waves along metal surfaces to localized electron oscillations on metal nanoparticles [33].

Nanoparticles can be small enough to allow an external electromagnetic field to penetrate into the volume of the particle and shift the free conduction electrons relatively to the particle's ion lattice. This results in a surface charge on the two opposite sides, with an opposite sign of the respective charge. These surface charges produce a restoring local electric field within the particle. The combination of charge shift and restoring electric field represents an oscillator that is defined by the electrons' effective mass and charge, the electron density and the geometry of the particle. Its resonances are called the surface plasmons [33].

The resonance frequency in a material can be found using a quasi-static approximation. This approximation is valid if the particles are small in comparison with local variations of the electromagnetic fields. The resonance frequency can be found when the polarizability α is maximal. For an ellipsoid, it is given by

$$\alpha = \frac{4\pi}{3} abc \frac{\epsilon_m - \epsilon_e}{\epsilon_e + A[\epsilon_m - \epsilon_e]} \tag{1.17}$$

where ϵ_m and ϵ_e are the frequency dependent dielectric functions of the metal and the environment. A is the depolarization constant and a, b and c are the ellipsoid's half axes. For spherical particles, $A = 1/3$ and the resonance frequency is where $\epsilon_m = -2\epsilon_e$ [33]. The resonance frequency is therefore dependent in the particle shape and size and the dielectric functions of the particle material and the environment. *E.g.*, gold nanospheres in water possess an absorption maximum that can be tuned between 520 nm for a diameter of 20 nm to 550 nm for a diameters of 80 nm [31, 32]. Other shapes such as core-shell structures or nanorods allow for tuning into the near infrared over a range of several hundred nanometres.

Once a surface plasmon has been excited, it has different pathways to relax. For larger particles, radiation damping, also called scattering relaxation, takes place. Electromagnetic waves are scattered as a result of the re-radiation of electromagnetic waves by the oscillat-

ing plasmon charge distribution. The energy needed for radiation is taken from the energy stored in a plasmon. For smaller particles, energetic relaxation, also called absorption relaxation, is the prevalent mechanism. Hereby the plasmons relax energetically through internal, *i.e.* ohmic, loss mechanisms and heat the metal nanoparticle. Baffou and Quidant found that gold nanoparticles are usually better absorbers than scatterers for sizes below $\approx$ 90 nm [31] but that the wavelength of excitation also plays a crucial role (*cf.* Figure 1.7).

The heating process itself is proposed to take place in three steps [31]. In the first step, electronic absorption takes place, exciting a surface plasmon. This process usually has a characteristic time in the range of $\tau_e \approx$ 100 fs and leads to a non-equilibrium situation. Secondly, absorption relaxation takes place: the electron gas cools down through electron-phonon interactions and thus heats the lattice of the nanoparticle. For nanoparticle sizes above 5 nm, this process is size-independent and has a characteristic time of $\tau_{e-ph} \approx$ 1.7 ps. The surroundings is still at its initial temperature. Only then, heat diffusion takes place. The characteristic time is dependent on the size of the nanoparticle and given by

$$\tau_{tr} \approx L^2 \frac{\rho \cdot c_p}{3 \cdot \kappa_s} \tag{1.18}$$

with L the characteristic length of the particle, ρ its mass density, c_p the specific heat capacity at constant pressure and κ_s the thermal conductivity of the surrounding medium. It is typically in the range of 100 ps to a few nanoseconds. Depending on the size of the particle and therefore the characteristic time of each process, they can also temporally overlap.

The power absorbed by a nanoparticles follows the simple equation

$$Q = \sigma_{abs} \cdot I \tag{1.19}$$

where σ_{abs} is the absorption cross-section of the nanoparticle and I the intensity of the incident electromagnetic radiation.
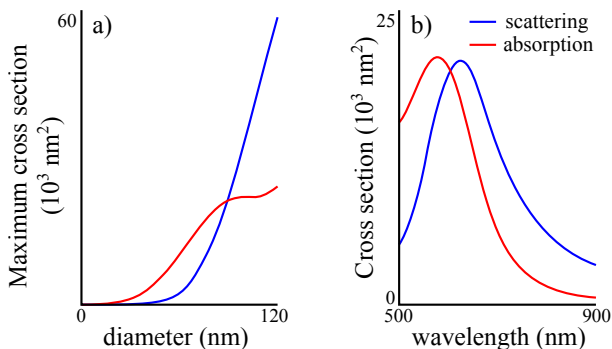
Figure 1.7: (a) Absorption and scattering cross sections for different gold particle sizes. Below 90 nm, absorption becomes the prevalent mechanism in extinction. (b) shows the cross sectiona of a spherical gold particle of diameter 88 nm as a function of excitation wavelength. Redrawn from [31].

1.4 MELTING POINT DEPRESSION IN GOLD NANOPARTICLES

The melting point is amongst the properties that drastically change when decreasing particle sizes. In 1909, Pawlow theoretically predicted this phenomenon called melting point depression, stating that the melting point of gold nanoparticles should decrease drastically down to room temperature for sufficiently small particle sizes. It took until 1956 to be confirmed

experimentally and has been widely studied for various particles, *e.g.* gold [34] or aluminium [35], but also other metals.

Melting point depression has its origin in the increasing ratio of surface to volume when decreasing particle sizes. In general, for the ratio $A/V = N^{-1/3}$ holds, where A is the surface, V the volume and N the number of particles. Because of the surface atoms usually are low-bound compared to the bulk, a surface excess energy exists. Therefore, less additional energy for melting is needed, which is why melting is proposed to start at surfaces or interfaces. As the A/V ratio increases, the surface excess energy gets larger and a melting point behaviour according to

$$T_m = T_m^0 \cdot (1 - \frac{X}{D}) \tag{1.20}$$

holds, with T_m^0 the melting point of bulk material, D the diameter of the particle and X a factor representing the magnitude of the depression with size. Figure 1.8 shows a plot of the melting point for gold particles *vs.* the reciprocal size. The straight line shows the predicted $1/D$ behaviour as a guide to the eye. The melting points seem to match very well to the prediction, except for very small sizes where the spread becomes significant. The expected melting points of the nanoparticles used in this work are shaded in red.

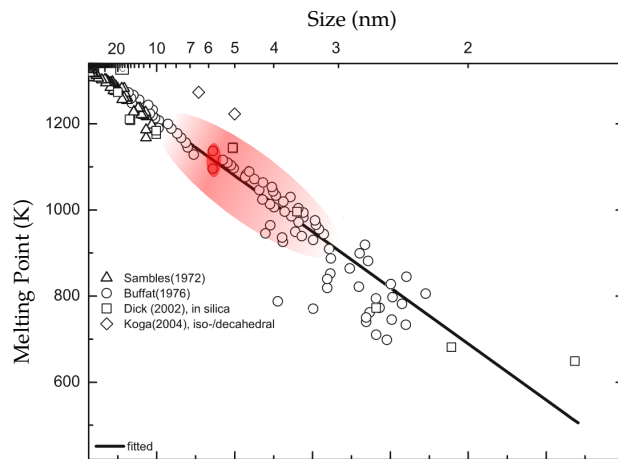Figure 1.8: Size-dependent melting of gold nanoparticles down to 1.5 nm. Comparison of experimental values of various studies with different techniques. The straight line is a fit by (1.20) as a guide to the eye. The small oval in red depicts the range of mean particle diameter for all samples used in this work. The larger oval shows the area of any particle size that occurred in any sample. With variations taken from [36].

EXPERIMENTAL

2.1 DEVICES

2.1.1 *Scanning Transmission Electron Microscopy*

To verify the attachment of the gold nanoparticles on the nanorods and to rule out the clustering of gold nanoparticles, scanning transmission electron microscopy was used. A Hitachi SU-70 was used at an accelerating voltage of 30 kV in transmission geometry.
A small amount of powder was thoroughly dispersed in demineralised water. Copper grids spanned by a thin carbon film were dipped into the dispersion using tweezers and gently moved in the dispersion. They were then left to dry in air.

2.1.2 *Transmission Electron Microscopy*

In an attempt to investigate the behaviour of the gold nanoparticles upon heating to the onset of black body radiation, a Hitachi H9000-NA transmission electron microscope (TEM) was used at an accelerating voltage of 300 kV. The preparation was the same as above. The TEM was used in image mode only at a magnification of either 50 000 or 70 000.

2.1.3 *X-ray Diffraction*

To determine the phases before and after the calcination of the pure particles, x-ray diffraction (XRD) was used. Spinning powder samples were measured on a PANalytical Empyrean in Bragg-Brentano geometry using a copper anode (1.540 Å) without monochromator.

2.1.4 *Photoluminescence Spectroscopy*

For the photoluminescence spectrometry (PL) a Horiba Fluorolog TCSPC was used, equipped with a Horiba Jobin Yvon *i*HR320 monochromator. Samples were excited by a near infrared laser diode emitting at 980 nm (Roithner Lasertechnik, RLT981000G) in a Thorlabs LDM21 laser head. Laser current and cooling were provided by a LDC 220 and TED 200, both from Thorlabs, respectively. All experiments were conducted in the focal plane of the laser, with the sample tilted $\approx 55°$ with respect to laser axes.

2.1.5   *Inductively Coupled Plasma Optical Emission Spectroscopy*

To connect the nominal gold concentration of each sample to the actual amount of gold present, inductively coupled plasma optical emission spectroscopy (ICP-OES) was used. Small amounts of powder of the samples 2.5, 3.5, 5.0 and 12.5 have been investigated. Small amounts of sample powder were dissolved in aqua regia. Samples 25 and 37.5 have not been analysed by ICP-OES.

2.2   EXPERIMENTAL PROCEDURES

2.2.1   *Sample preparation*

Preparation of Oxide Nanorods: Solutions of 0.4 M ytterbium (Yb), 0.4 M gadolinium (Gd) and 0.1 M erbium (Er) were prepared by dissolving their nitrates in concentrated nitric acid (65%). 9.5 ml of the Gd solution, 0.3 ml of Yb and 0.8 ml of Er were mixed in a round bottom flask. Approximately 40 ml of water were added. 30.0 ml of a 25 wt-% solution of ammonia (NH_3) in water were added slowly under stirring. The flask was subsequently immersed in a ultrasonic bath for 5 min to disperse the forming nuclei. After sonication, the flask was immersed in an oil bath at 70°C under constant stirring for 16 hours.
The grown particles were washed five to ten times with demineralised water. In the last cycle, they were again sonicated to better disperse them and subsequently centrifuged to get rid of the water. They were then washed in ethanol and dried at 75°C.
The dried product was ground to a fine powder in a mortar and calcined at 700°C for 180 min.
Growing Gold Nanoparticles directly onto the Nanorods: In a typical synthesis, a 250 ml flask was cleaned with freshly prepared aqua regia and sonication in water. 100 mg of previously calcined nanorods were added and dispersed in at least 120 ml distilled water under sonication for 15 min. 2.000 ml of a 0.01 M gold(III) chloride trihydrate ($HAuCl_4 \cdot 3H_2O$, Sigma-Aldrich) solution were added. The solution was left under stirring for 120 min.
Subsequently, 1.28 ml of a 0.1M $NaBH_4$ solution were quickly added under vigorous stirring. The solution immediately turned purple. The solution was then left for approximately 10 min for reaction. Finally, the particles were precipitated by centrifugation and washed.
In general, the gold content varied, while the ratio quantity of gold to volume of $NaBH_4$ solution remained the same. The particles were given the name *X*, where *X* was the nominal amount of gold in micromols per 25 mg of nanopowder in the initial reaction solution.

In total, six samples were analysed. Their names and μM of gold per 25 mg powder were 2.5, 3.5, 5.0, 12.5, 25, 37.5.

2.2.2   *Photoluminescence Spectroscopy*

Spectral acquisition: For the acquisition of spectra, the laser current was set on the current controller and left unchanged until the spectrum had been acquired. Typical acquisition times ranged from 30 secs to 5 mins, depending on the emission intensity from the sample and the wavelength increment. Spectra were acquired in the range from 350 nm to 750 nm.
Continuous acquisition: To determine the values of the onset of the blackbody radiation, the spectrometre was used in constant acquisition mode and the laser current slowly increased. The current laser current and the emission intensity were monitored simultaneously using a camera. Emission was monitored at 710 nm, which was in the region where the black body

radiation usually set on, while being spectrally far enough away from both the laser artefacts (down to until ≈ 750 nm) and the erbium emission around 660 nm.

Laser Calibration: To measure the laser output power as a function of the laser current, the laser was used out of focus onto a Coherent OP-2 VIS silicon optical sensor. The laser was guided in a structure of aluminium foil in order to collect all laser power despite the distance between laser and sensor being far away from the focal length of the laser optics. The output laser power was measured in the regime covered by the sensor and interpolated in between. To increase the laser current range accessible, neutral density filter of ND = 1.0 and ND = 2.0 were used. Acquisition was performed at 976 nm, the nominal emission wavelength of the laser diode according to the manufacturer.

Sample Preparation: Samples for PL were prepared in two different ways.
Pressure deposition: A small copper plate was covered in a very thin layer of vacuum grease, a small amount of powder put onto it and firmly compressed onto the plate with a spatula.
Dispersion deposition: Powder was immersed in acetone in a ratio of 10 μl acetone per mg of powder. Sonication for approximately 15 mins was performed to guarantee good dispersion. Between 10 and 15 μl of this dispersion when then dripped onto a little copper plate of ≈ 5x5 mm. It was made sure that the droplet did not exhibit a strong surface curvature, which would have led to cracks in the surface upon drying. When the acetone had dried off in air, the samples were put in the oven at 75°C for 15 mins to completely evaporate the acetone.

Influence of the Sample Preparation: A comparison was made between the two variations of sample preparation for PL. A sample was prepared with each method described above and the onset of the black body radiation measured for various spots on each sample in continuous acquisition. Both samples were mounted simultaneously to avoid influences of the tilt of the support and switched by sliding the samples on the support. The laser current was increased until the sharp increase in the luminescence intensity at 710 nm became apparent. No spot was used twice. Spots in inhomogeneous samples were chosen in regions that appeared to be the most homogeneous.

Influence of the Laser Heating on the Sample Morphology: In an attempt to clarify the behaviour of the nanorods and the nanoparticles under illumination, sample powder 5.0 was exposed to different laser power densities. Scanning transmission electron microscopy (STEM) images were taken for unexposed powder, powder that had been exposed to a laser power density just above the black body radiation threshold and to a power density high above the threshold.

To reveal the influence of the laser heating on the emission properties, powder of sample 12.5 was cyclically illuminated three times. Each time, the laser power density was increased until the emission intensity was strong enough to be easily seen by the naked eye, and decreased again. Both laser current and emission intensity at 710 nm were acquired simultaneously.

2.2.3   *Temperature Sensing procedures*

Both temperature sensing procedures were only used in the regime where more or less pure spectra were obtained. Usually there existed a region where both the erbium emission and the black body radiation where observed, yet the spectra could not be properly deconvoluted and results were thus not reliable.

Calibration and Use of the Fluorescence Intensity Ratio: Equation (1.5) was used to determine the temperature from the fluorescence intensity ratio (FIR), however, ΔE and B had

to be determined. For this, undecorated calcined nanorods were used. Spectra were recorded in the region of the emission from the thermally coupled states $^2H_{11/2}$ and $^4S_{3/2}$ between 500 nm and 590 nm for different laser powers. For the emission from $^2H_{11/2}$ and $^4S_{3/2}$, integration limits were chosen from 510 nm to 540.5 nm and 540.5 nm to 567 nm, respectively. The ratios of intensity were plotted in a FIR *vs.* laser current plot. The equation $y = a \cdot x + b$ was fitted to the data in the linear regime of the ratio and the value of b was assumed to be the FIR at room temperature. To determine the energy splitting ΔE, the precise spectral positions of the peaks at $\approx$ 536 nm and $\approx$ 560 nm were determined and the energy difference expressed in wavenumbers. Boltzmann's constant was taken from literature as 0.695034 cm^{-1}. B was calculated by solving (1.5) for B and using the obtained values.

If (1.5) was used, slight changes in the peak positions were accomodated by changing the integration ranges accordingly. Values for B and ΔE as previously obtained from the calibration procedure were used to determine the temperature by solving (1.5) for T.

Determination of the Temperature by Fitting of the Planck Law: For higher temperatures, the erbium emission lines became increasingly noisy and eventually vanished in the spectrum of the black body radiation. For pure black body emission spectra, the temperature was determined by fitting Planck's law (1.13) to the spectrum. (1.13) was extended by adding a factor that accounted for the constant noise, especially useful for spectra at lower intensities, *e.g.* when the spectrometre slits had been narrowed. The equation for fitting finally read:

$$I(\lambda, \boldsymbol{y_0}, \boldsymbol{A}, \boldsymbol{T}) = \boldsymbol{y_0} + 8\pi hc \cdot \left\{ \frac{\boldsymbol{A}}{\lambda^5 \cdot \left[\exp\left(\frac{hc}{\lambda k \boldsymbol{T}} \right) - 1 \right]} \right\}, \tag{2.1}$$

with $h = 6.62606957 \cdot 10^{-34}$, $c = 2.99792458 \cdot 10^8$, $k = 1.3806488 \cdot 10^{-23}$ and λ in meters (units were deliberately neglected); the fit parameters are in bold-face type.

The second half of the r.h.s of (1.13) has been reduced to look more clear. Compared to literature [20], the factor in front of the curly brackets differs. However, as the actual intensity was not of interest here, it was not important. It could also have been omitted entirely and absorbed into the factor A. The factor y_0 was mostly used for spectra at lower temperatures, when the noise made up a significant part of the spectrum. For temperatures (from fit) of around 1100 K and above, the difference in the results with or without the factor were at most 1.5 K. Fits were done from 350 nm to 633 nm.

RESULTS AND DISCUSSION

3.1 CHARACTERISATION OF THE SAMPLES

3.1.1 *X-ray Diffraction*

X-ray diffraction (XRD) was performed to confirm the transformation from the as-produced gadolinium hydroxide into the desired gadolinium oxide during the calcination process. Figure 3.1 shows the XRD spectra before and after calcination. As can be seen, the transformation has been complete. The peaks of the powder are shifted towards higher angles both in the non-calcined as well as in the calcined powder.
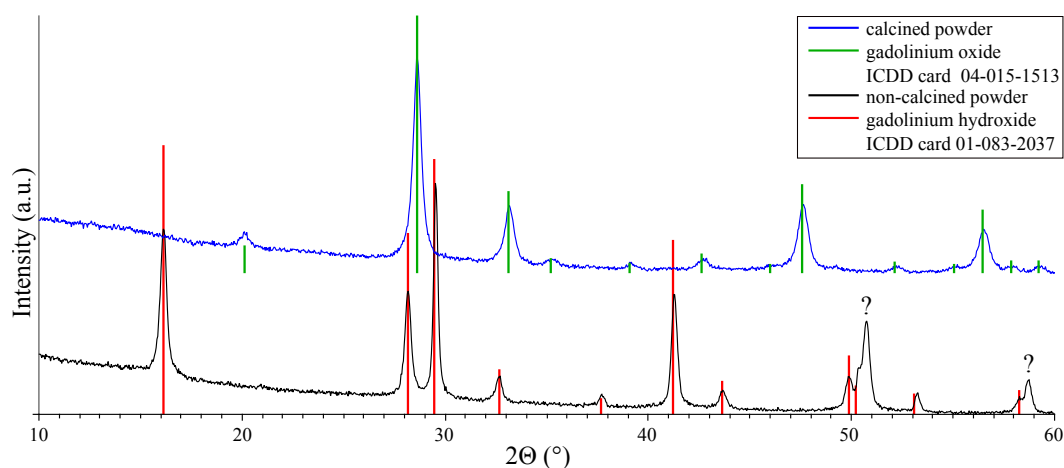

Figure 3.1: X-ray diffractograms of non-calcined and calcined powders. The vertical lines are the x-ray reflexes as given by the respective ICDD powder diffraction cards.

The corresponding slightly smaller crystal plane distance is most possibly related to the doping with erbium and ytterbium, both posses ionic radii smaller than gadolinium [37]. The two peaks labelled with a question mark are unidentified, their origin is unknown.

3.1.2 *Scanning Transmission Electron Microscopy*

Figure 3.2 shows transmission electron microscopic (TEM) images of each sample used in this work. The number of gold particles increases from (a) to (f) as expected. Especially for low gold concentrations, the number density seems inhomogeneous with some rods covered well while others are blank. As confirmed as well by scanning transmission electron microscopy, all gold particles are well-attached to nanorods. From all TEM images of each sample, the size of the gold nanoparticles has been determined by image analysis and is shown in an

inset in the respective image. The nanoparticle diameters were approximately constant, with an average diameter between 5.5 nm and 6.1 nm. Sizes ranged from 3 nm to 12 nm.
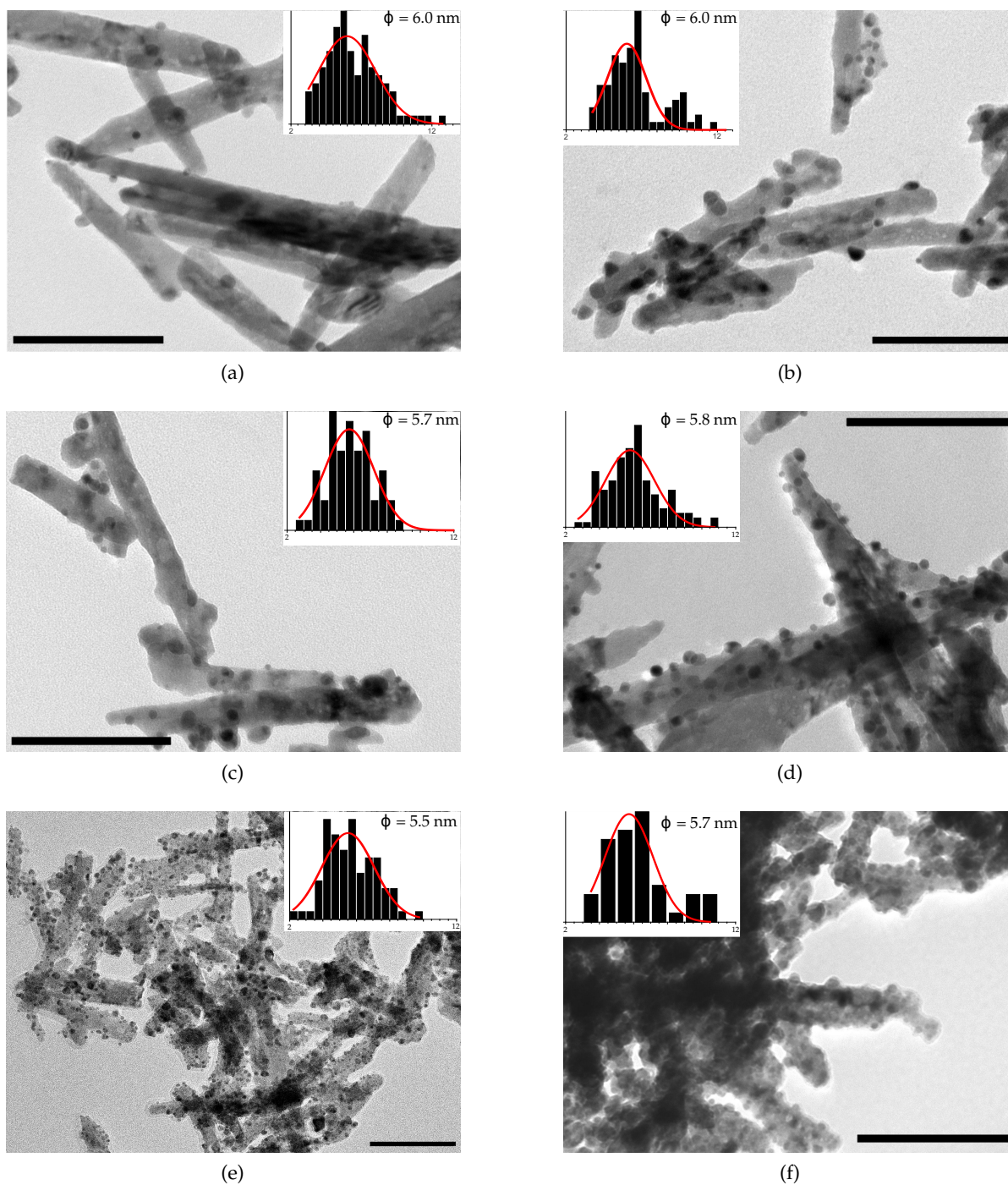

Figure 3.2: Transmission electron micrographs of the samples used in this work. (a) sample 2.5, (b) sample 3.5, (c) sample 5.0, (d) sample 12.5, (e) sample 25, (f) sample 37.5. The oxide nanorods decorated with gold nanoparticles are clearly visible, the latter appear as dark spots or protrusions from the otherwise smooth nanorod surface. The black bars corresponds to 100 nm. The insets in each image depict the diameter *vs.* size counts for the gold nanoparticles in each respective sample. On the bottom, the average diameter as determined from a Gauss fit (red), is noted.

From the average diameter, a melting point of around 1100 ± 50 K would be expected. The smallest particles might start melting already at around 750 K (*cf.* Section 1.4). Only very few particles of this size were found, however. Comparing the sizes with the theory (*cf.* Section 1.3) leads to the conclusion that the nanoparticles on the nanorods should exhibit excellent absorption properties and low scattering.

3.1.3   *Inductively Coupled Plasma Optical Emission Spectroscopy*

Inductively coupled plasma optical emission spectroscopy (ICP-OES) was performed twice on the samples 2.5, 3.5, 5.0 and 12.5 in order to verify the actual gold content. Table 3.1 lists the results. It is important to note that the results possess an inaccuracy of $\approx 15\%$. The actual gold content increases with increasing gold content in the reaction solutions. As the samples 25 and 37.5 have not been analysed by ICP-OES, the gold concentrations in their reaction solutions was taken as the gold concentration in the sample and calculated to mass percent. In the following text, the samples will be referred to as their sample name followed by the

Table 3.1: Elemental analysis results obtained from inductively coupled plasma optical emission spectroscopy. The values possess a possible inaccuracy of $\approx 15\%$. The values with an asterisk (*) are not measured but calculated.

Sample Name	Mass percent			
	Gold	**Gadolinium**	**Erbium**	**Ytterbium**
2.5	1.2	75.5	1.9	2.6
3.5	2.5	78.3	2	2.7
5.0	2.4	73.7	1.9	2.5
12.5	3.6	75.7	2	2.5
25*	16.5*			
37.5*	22.8*			

gold concentration in mass percent. For this, only the mass percent relative to the sample mass will be counted and it will be declared by a %-sign behind the number.Plots of some propertie *vs.* the gold concentration will consider the ICP-OES vcalues only. In consequence, this means that despite originating from a reaction solution of higher gold concentration, the sample 5.0 has in fact a lower gold concentration than sample 3.5/2.5% and will be plotted accordingly. It is also interesting, that the gold concentration in the samples does not increase at the same rate as the gold concentration in the reaction solutions. The values calculated for the samples 25/16.5% and 37.5/22.8% have thus to be considered with great care when deriving conclusions.

3.1.4   *Temperature Calibration of the FIR*

Determination of the energy splitting: The resulting splitting was determined as

$$\Delta E = (802.47 \pm 4.73) \text{ cm}^{-1},$$

which is on the upper end of what has been reported in literature, but still in the known range for erbium (*cf.* Section 1.2.1).

   Determination of B: The FIR was determined for every spectrum by integration as described in Section 2.2.3. The result is shown in Figure 3.3. Room temperature at the time of the measurements was 296 K (23°C). Fitting was done in the linear regime, once from 290 mA to 610 mA, and once from 370 mA to 610 mA. For each fit, FIR at zero laser power was determined and read

$$FIR_{290}(0 \text{ mA}) = 0.26338 \quad \text{and} \quad FIR_{370}(0 \text{ mA}) = 0.26314,$$

respectively. From (1.5) followed a value of

$$\ln B_{290} = 2.5645 \quad \text{and} \quad \ln B_{370} = 2.5636.$$

This lies within the values for B reported in literature (*cf.* Section 1.2.2). For later temperature calculations, $\ln \bar{B} = 2.564$ was used.
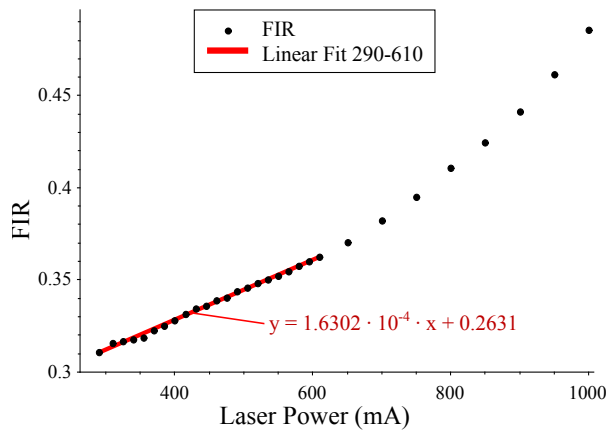

Figure 3.3: FIR and linear fit for calibration of the temperature sensing. Only the fit in the region from 290 mA to 610 mA is shown here. The fit is labelled with an equation $y = a \cdot x + b$.

3.2   EVALUATION OF THE EXPERIMENTAL CONDITIONS

The preparation of the samples as well as the experimental setup had a strong influence on the results in this work. To give the reader an impression of the precision limits of any laser power density dependent results, the following paragraphs present the error sources as well as the expected relative errors thereof.

   Influence of the sample preparation for photoluminescence spectroscopy (PL): Experiments were conducted in the way described in Section 2.2.2. The results can be seen in Figure 3.4. The range in which the black body radiation sets on is significantly larger for a pressure deposited sample compared to a dispersion deposited. Optical images of the samples (*cf.* Figure 3.4b) reveal strong inhomogeneities in colour. The onset of the black body radiation is found to vary by $\approx \pm 12\%$ around the mean value. On the other hand, the variation of the dispersion deposited samples is only $\approx \pm 4\%$ around the mean value. The sample optically looks much more homogeneous. In fact, on some dispersion deposited samples, no spread

of the onset value at all had been observed, while for some pressure deposited samples variations of as much as 40% were observed. They are not shown here because comparable studies were not done.
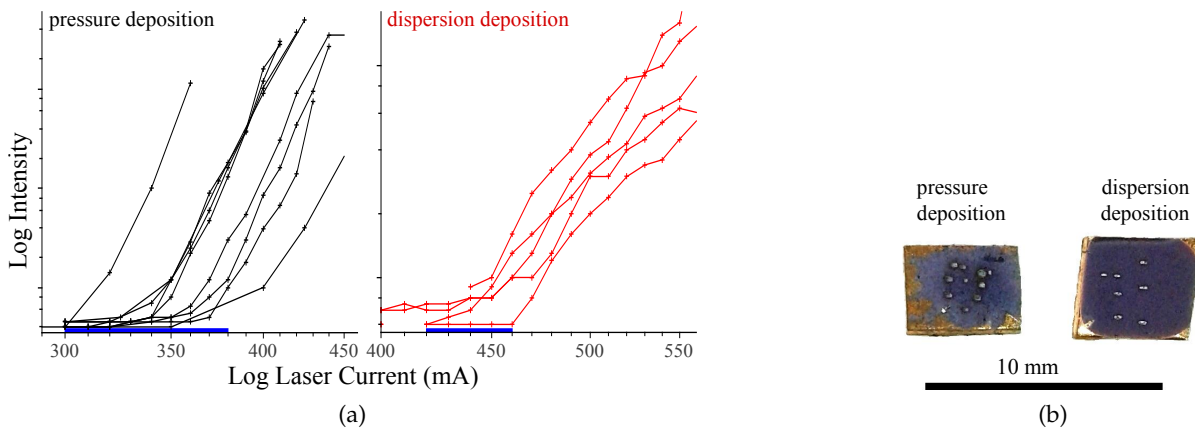

Figure 3.4: Comparison in properties between pressure and dispersion deposition. (a) ranges of the onset in black body radiation (thick blue line). The x-axis covers the same range of laser powers for better comparison. (b) optical images of samples. The gray spots have been irradiated with high laser powers to mark already used spots.

The wider spread for the pressure deposited samples probably stems from the significantly different degree of compaction between the middle (dark purple) and the edges (light purple) of the sample. Due to the varying porosity, the density of heating elements, *i.e.* gold nanoparticles, varies and leads to varying heating efficiencies, thus the random behaviour of the powder. On the other hand, the degree of compaction of the dispersion deposition should be mostly determined by the ratio of powder to dispersant and the nature of the dispersant instead by the position on the sample. The difference in the laser power that is needed to achieve the onset can, too, be explained by differences in the porosity.

It is therefore better to produce samples by the dispersion method and make an effort to control the ratio of powder to dispersant. It must be made sure that the sample shows no cracks in the surface and that all the sample is well attached to the copper plate. All results in this work are, unless mentioned otherwise, from dispersion deposited samples.

Error from the Excitation setup: The other main error source during the excitation experiments stems from the position of the sample and laser with respect to each other. A detailed theoretical analysis can be found in Section A.2. Assuming that the sample can be oriented with a precision of $\approx 5°$ with respect to the desired position of $55°$ and that the laser spot area is out of the best attainable by a maximum of 30%, an estimated error of 33% should be expected.

Spectral Range of Fits for Black Body Temperatures: Spectra were acquired from 350 nm to 750 nm. Two different wavelength ranges were tried for fitting of the black body radiation (*cf.* Figure 3.5). The original spectrum data is drawn in blue. The fits are drawn in black and red for the fit range of up to 750 nm and up to 633 nm, respectively. In the linear plot, the deviation of the black fit curve from the spectrum is visible for the spectral range above 500 nm, while the red fit virtually hides the measurement data. The logarithmic plot reveals a distinct misfit for shorter wavelengths than 500 nm for the black fit. Compared to this, the red fit only deviates at very low wavelengths below 420 nm. The stronger deviation of the black

fit is also represented in the respective coefficients of determination. While the red fit shows an excellent fit with $R^2 = 0.999913$, the black fit possesses a coefficient of determination of only $R^2 = 0.996817$.

Fits in a wavelength range up to 633 nm are therefore better. The misfit at short wavelengths of both black and red fit is due the nature of the fit that tends to y_0 for low wavelengths, which in this case was fixed to zero, the fits otherwise diverged. The value of 633 nm itself was chosen because it avoided influence from the erbium emission around 660 nm that often persisted until higher temperatures.
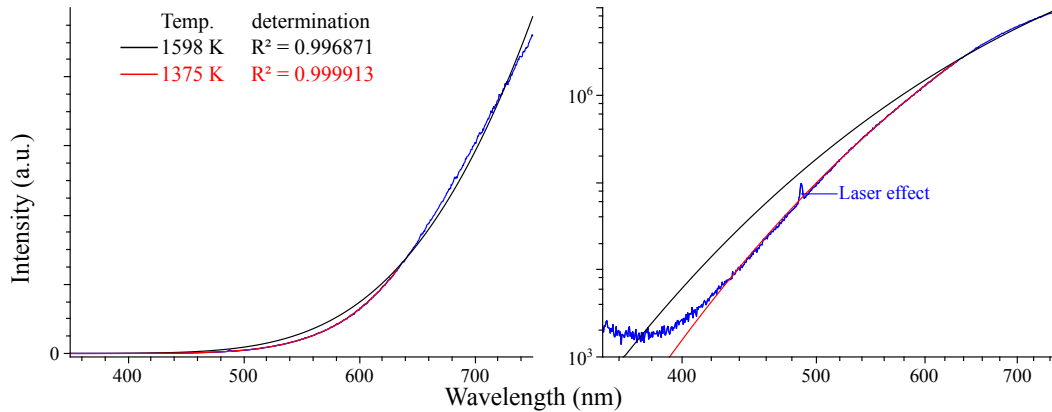

Figure 3.5: Comparison of fir ranges. The left graph shows a linear plot of a spectrum, the right a double-logarithm plot of the same data. The blue jagged line is the spectrum as measured, the smooth black and red lines are the fits, labelled with the resulting temperatures. The much better match for the fit up to 633 nm (red) is apparent. The fit over the entire range (black) shows visible deviation from the spectrum. The coefficients of determination are given. The notch at 488 nm is a laser effect, probably a reflection of the second harmonics generation.

The worse fit when including higher wavelengths is due to the almost linear behaviour of the spectrum above 650 nm. The reason for it is unknown, this may stem from an overlay of the erbium emission on the black body radiation. Further investigation into this was not done. All fits were performed only until 633 nm for this reason.

3.3   THRESHOLD OF THE BLACK BODY RADIATION

The threshold of the black body radiation as a function of laser power density was measured in two ways, described in Section 2.1.4. For the samples 25/16.5% and 37.5/22.8%, black body radiation was observed even for the lowest laser power densities, the threshold value has therefore been set to zero.

Figure 3.6 shows an example of the spectral acquisition method, data for continuous acquisition and the resulting threshold values for the required power density to trigger black body radiation as a function of gold concentration for both methods. As can be seen, both methods show the same trend, an approximately exponential decrease in the threshold with an increasing gold concentration. However, the values of the two methods differ by sometimes as much as 30%. This might be due to an experimental error as described in Section 3.2 or due to the increased heating time of the spectral compared to the continuous acquisition. While the spectral acquisition keeps the samples at the each laser power for several minutes,
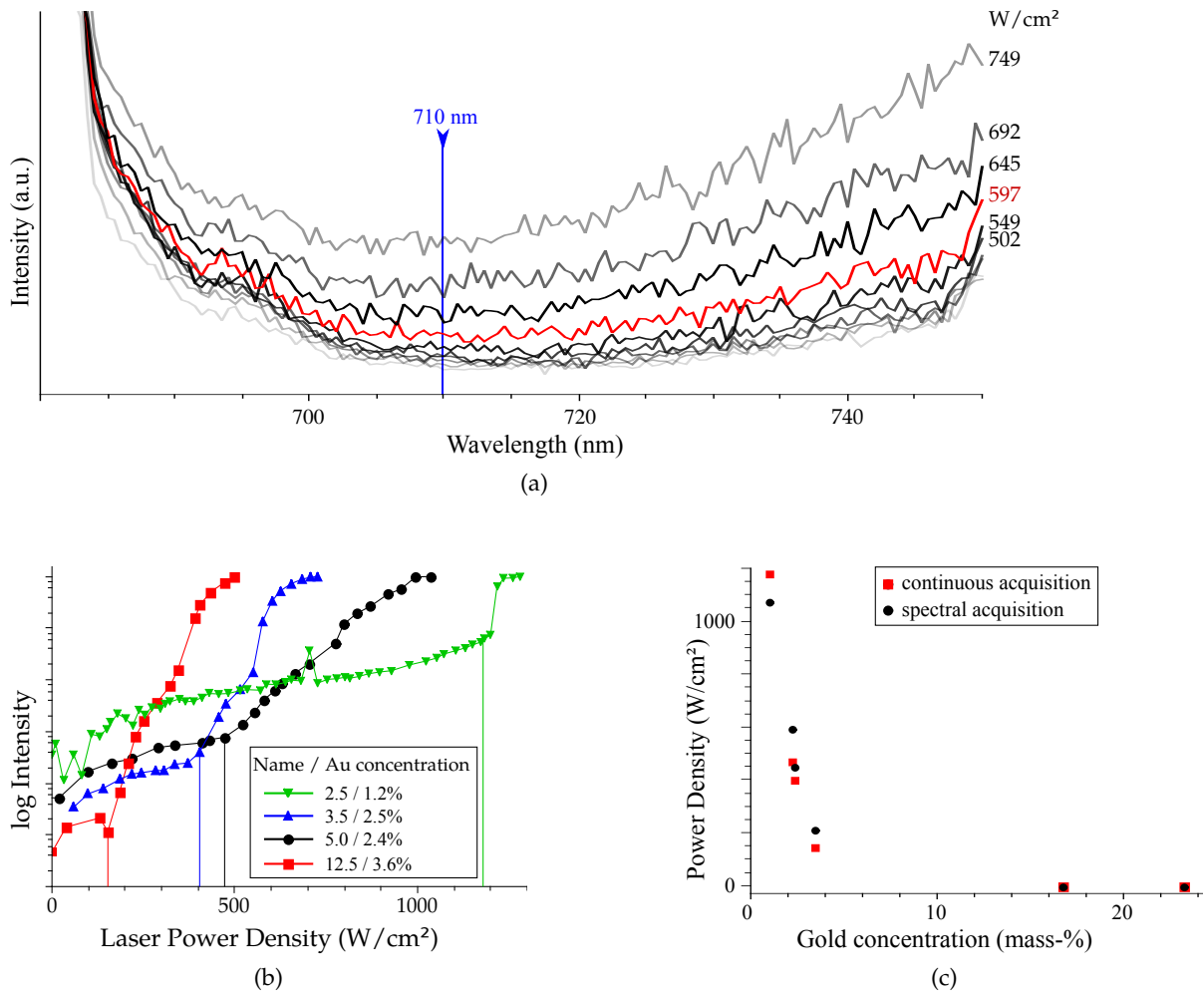
Figure 3.6: (a) Exemplary spectra of the sample 5.0/2.4%. Only the spectral parts relevant for the spectral determination of the radiation threshold is shown. The black body radiation sets on around 597 W/m² (red spectrum). The other spectra are shown for comparison. The blue arrow shows the acquisition wavelength for the continuous acquisition wavelength.
(b) Continuous acquisition curves for four different samples. The threshold of the black body radiation is sketched in vertical lines of the respective colours.
(c) Plot of the laser power density needed to trigger black body radiation as a function of the gold concentration in the sample for both continuous and spectral acquisition. The values of 25/16.5% and 37.5/22.8% were chosen as zero because a transition from some luminescence to black body radiation was not observed.

the continuous acquisition takes usually place in a timespan of 30 secs. However, the heating below the threshold will be shown to have no effect on the samples (see below). For the threshold at of the sample 2.5/1.2%, an additional difficulty was to determine it from the spectral acquisition as there was no really clear offset beginning at a certain power density. The value chosen was the first value at which this was clearly the case, which in turn means that the actual onset might be even lower.

The continuous acquisition method thus is the better of the two methods for several reasons. It is much less time-consuming during the measurements. Additionally, the equipment can be reduced to a fixed-wavelength monochromator. On the other hand, difficulties arise for samples that require very high laser powers, because acquisition of the intensity at a certain

wavelength tells nothing about the nature of the luminescence. One might thus confuse the reflected laser intensity for black body radiation.

3.4 BEHAVIOUR OF THE MORPHOLOGY UNDER ILLUMINATION

In an attempt to clarify the behaviour of the nanorods and the nanoparticles under illumination, sample powder 5.0/2.4% was exposed to different laser power densities. The scanning transmission electron microscopy (STEM) images are shown for unexposed powder (Figure 3.7 (a), (b)), powder that had been exposed to a laser power density just above the threshold (Figure 3.7 (c), (d)) and to a power density high above the threshold (Figure 3.7 (e), (f)). If present, the gold nanoparticles on the rods are visible as black small dots.

 From the STEM images it is apparent that the heating seems to deform a part of the particles. While the powder that underwent only the onset of the black body radiation seems to not have changed and the gold nanoparticles seem still intact, Figure 3.7e show particles that seem to have somehow molten together, visible by the lack of contrast between single particles and the rounded corners. However, it is also visible that not all particles underwent this transformation (Figure 3.7f). The gold nanoparticles have disappeared on the molten nanorods, whereas they are still visible on the non-transformed parts.

Spectra were aquired under the same conditions to confirm the temperatures by fitting with black body radiation. Temperatures were determined to reach up to 1500 K when the laser power density was at its maximum.
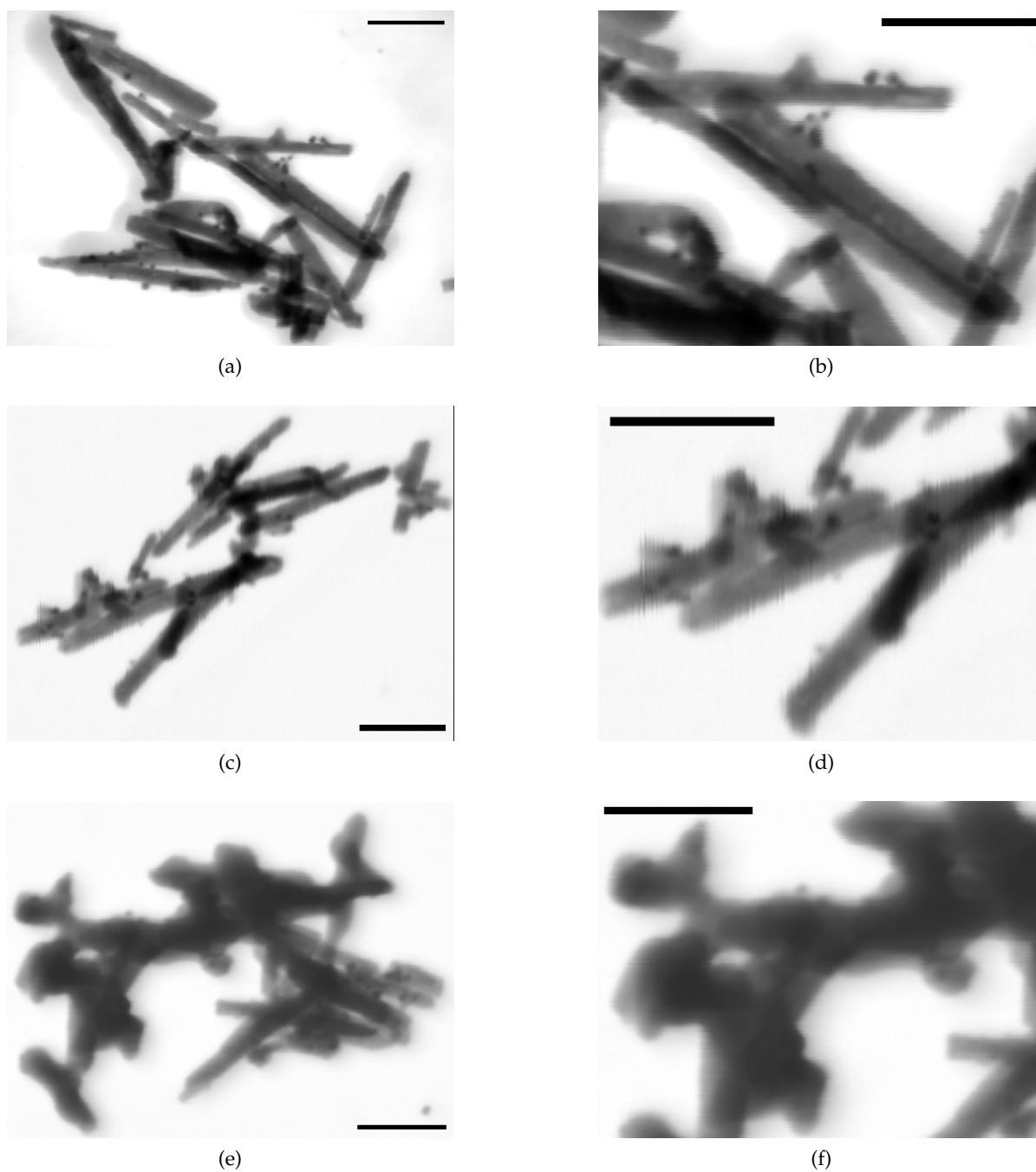
Figure 3.7: Scanning transmission electron micrographs of sample 5.0/2.4%. The gold nanoparticles are distinctly visible on the rods as small black points. The black bars correspond to 100 nm. The images on the right are magnifications of the respective left images.

(a) and (b): Sample after decoration with gold nanoparticles.

(c) and (d): Sample after undergoing excitation at a power density just above the black body radiation threshold. The sample shows no apparent change.

(e) and (f): Sample after strong excitation at a power density way above the threshold. The sample shows visible loss of gold nanoparticles (left). Additionally, parts of the nanorods show significant clustering and rounded edges from the sintering process.

Threshold Values for Repeated Illumination: To investigate at which power density the transformation set in, illumination in repeated cycles was conducted on sample 12.5/3.6%. Figure 3.8 shows the results of the cyclical continuous acquisition. The upper graph shows the intensity if the laser power is increased far above the threshold value every cycle, the lower two graphs depict the same if the laser power is held just above the threshold. In the first case, it is clearly visible that the threshold of the black body radiation increases with every cycle. For laser power densities kept low, the threshold seems not to change notably.
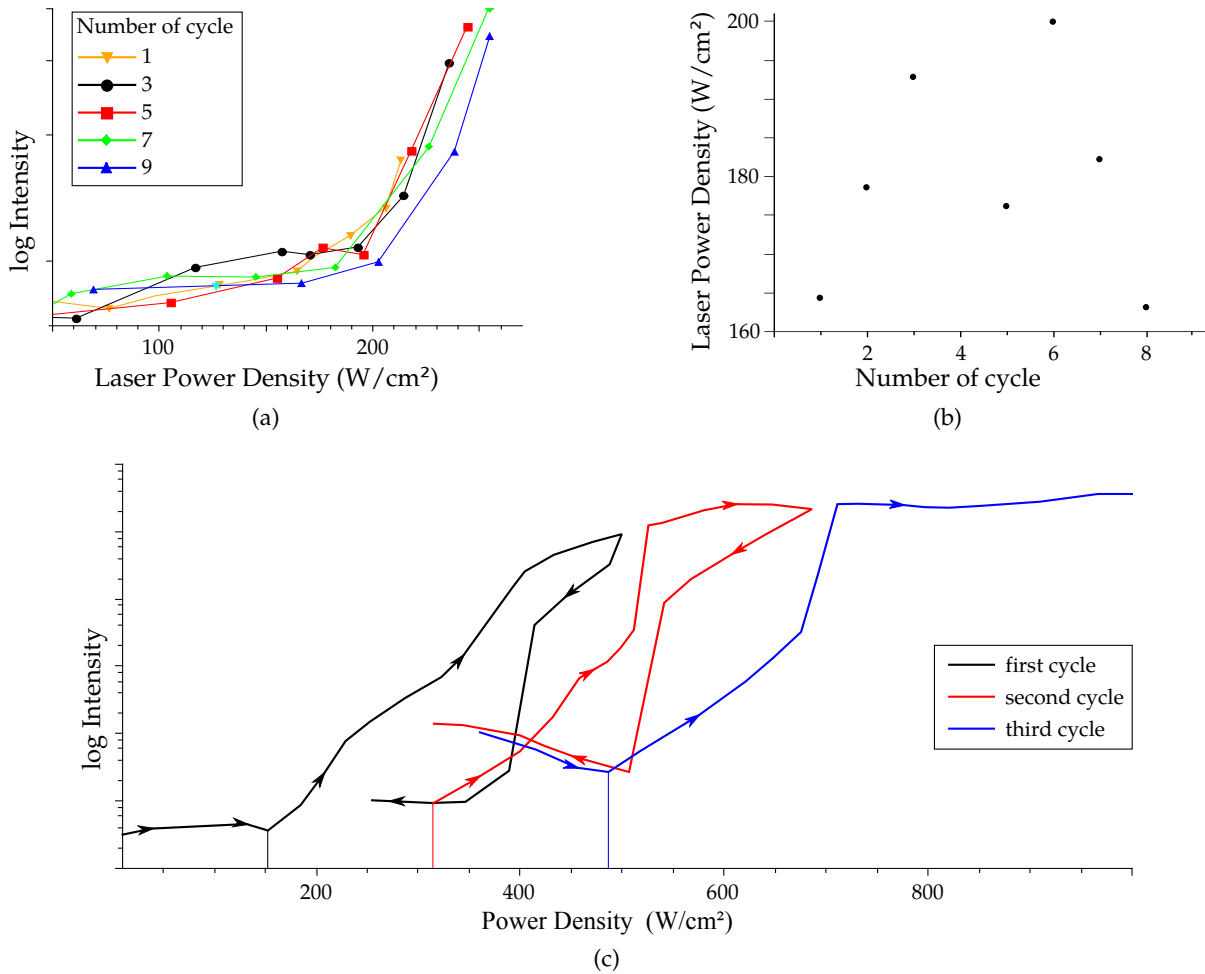

Figure 3.8: Evolution of the emission intensity at 710 nm under repeated illumination. (a), (b) The laser power density was only increased until slightly beyond the threshold and held for 5 seconds before decreasing. The threshold values show no visible trend. (c) The sample was illuminated with a laser power density high enough to trigger bright black body radiation. The respective thresholds are denoted by thin lines connecting the curves with the x-axis. The temporal direction of the intensity and power density are depicted by arrows.

Temperature at the Threshold: To get an idea of the actual temperature at the threshold, it was calculated from the FIR. Figure 3.9 shows the result. In this case, data from both dispersion and pressure deposited samples was used. For the dispersion deposited samples, the temperatures show a wide spread over a range of 100 K, the spread of the pressure deposited samples is about 85 K. Due to repeated measurements, more data was available
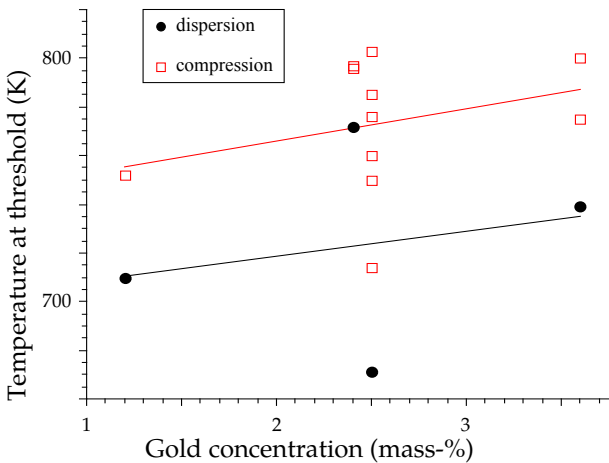
for the pressure deposited samples.

Figure 3.9: Local temperature at the black body radiation threshold as a function of the gold concentration. Black dots represent data from the dispersion deposited samples, empty squares data from the pressure deposited samples. Straight lines are linear fits. Parameters are given in the text.

A linear fit to the dispersion data yields $T_{disp} = 689.1\,\text{K} + 10.25\,\text{K} \cdot c$, where c is the concentration of gold in mass percent. The coefficient of determination is only $R^2 = 0.05487$. The linear fit to the pressure data yields $T_{pres} = 739.5\,\text{K} + 13.26\,\text{K} \cdot c$ with $R^2 = 0.09569$. In average, the temperature at the threshold is $\bar{T} = (760 \pm 38)\,\text{K}$. While a trend might really exist, it is impossible to tell with certainty from this data. The coefficients of determination are far too low to allow for a reliable result.

It is remarkable that the average temperature at the threshold is higher for the pressure deposited samples compared to the dispersion deposited samples.

Elemental Distribution After Ilumination at a Power Density Well Above the Threshold: In a previous work (courtesy of Dr. Mengistie Debasu, University of Aveiro), a sample powder has been pressed to a pellet and illuminated at a power density well above the black body radiation threshold. After this, scanning electron micrographs and an elemental analysis profile by energy dispersive x-ray spectroscopy (EDS) have been taken of an illuminated spot. The results are shown in Figures 3.10 and 3.11. The laser seems to have strongly altered the sample morphology, as can be seen by comparing the region within the blue circle with the outer region. In the middle, the sample shows a big crack. From the EDS profile in Figure 3.11
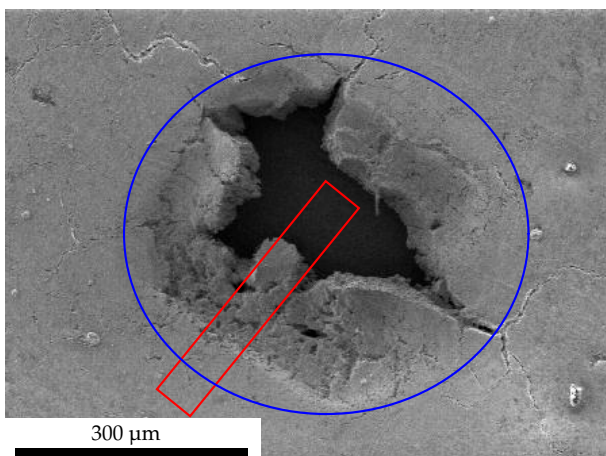

Figure 3.10: Scanning electron micrographs of spot analysed by energy dispersive x-ray spectroscopy. The blue circle roughly sketches the laser spot. The tilted red rectangle is the micrograph shown on the bottom of Figure 3.11

it becomes apparent that the gold concentration is strongly reduced in the spot covered by the laser whereas on the edges, a higher gold concentration can be found. The crack in the
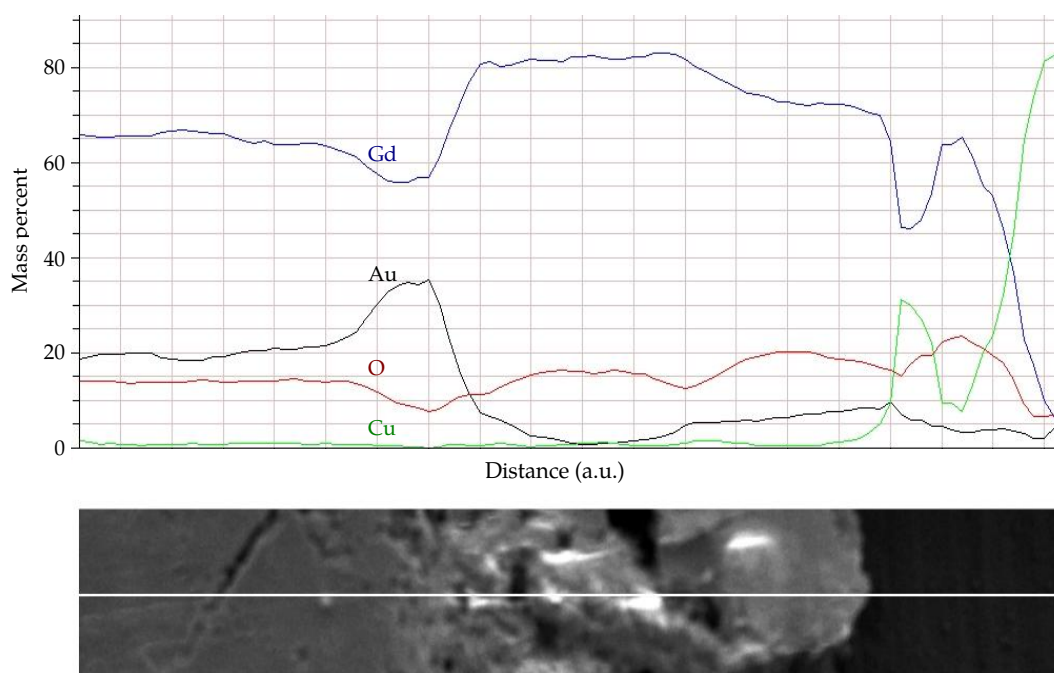
Figure 3.11: Elemental concentration profiles as obtained by energy dispersive x-ray spectroscopy. The white line in the bottom micrograph depicts the line where the scan was taken. The actual scan area with respect to the entire illuminated spot is depicted in Figure 3.10.

middle shows a strong copper signal, indicating that little to no powder covers the copper support anymore.

From the above results, several conclusions can be drawn. The onset of the black body radiation seems not to coincide with the melting of the gold nanoparticles. As can be seen from Figures 3.7c and 3.7d, the morphology of the rods does not change and the nanoparticles remain unchanged in sizes and number density. This is confirmed by the results from the repeated illumination. If the laser power density is kept at or only slightly above the threshold value, no change in the threshold itself is observed. This behaviour should be expected from previous results compared with Section 1.4, as the melting point of the nanoparticles used in this work should be around 1100 ± 50 K. The temperatures at the threshold laser power density on the other hand did never exceed 810 K which is obviously not enough to melt the particles. Only a tiny fraction of the gold nanoparticles might be affected at this temperature whose density is not enough to alter the macroscopic properties of the powder.

At high laser power densities, on the other hand, the heating is strong enough to heat the particles to temperatures at which the nanoparticles melt and even sintering processes between the nanorods set in. Almost no gold nanoparticles can be found on the nanorods that show significant clustering and rounded edges. From the EDS results it can be concluded that the gold is driven away from the laser spot and collects on the edge of the laser spot. The hole in the middle of the spot in Figure 3.10 might be due to the strong sintering of the particles that significantly reduced their porosity and thus the volume, backing the assumption that the rods are changing their morphology. However, it might also be that during the handling of the sample, some powder fell out due to thermally induced stresses during cooling down. Upon strong illumination, the samples also change their threshold value for the black body radiation (*cf.* Figure 3.8c). Considering that the onset of the black body radiation always seems to occur at the same temperature, the gold nanoparticles either lose

their capability for efficient heating, or, more likely, disappear from the irradiated spot. In the following cycle, a higher laser power density is then needed to achieve the same heating power, thus changing the threshold.

When talking about the temperatures at the threshold laser power density, Figure 3.9 must be interpreted carefully. It has to be considered that at the threshold of the black body radiation the determination of local temperature by both FIR and black body radiation is rendered difficult and that a certain error of unknown magnitude will result. In fact, despite that both fits seem to describe the same trend of increasing temperature at the threshold with the gold concentration, the error in the fits itself is too high to draw reliable results. Given the small number of data points and the large uncertainty in the fits, the temperature at the black body radiation threshold is more likely to remain the constant as a function of gold concentration. This assumption is backed up by the fact that the black body radiation is dependent only on the temperature and the surface emissivity of the sample. In this assumption, the possible change of surface emissivity by the variation in gold nanoparticle density is neglected. The black body radiation should therefore set in always at the same temperature.

3.5 HEATING EFFICIENCY AS A FUNCTION OF GOLD CONCENTRATION

More gold nanoparticles should result in a more efficient heating process. To confirm this, the heating efficiency as a function of the gold concentration was investigated. Linear fits were done in the low power, linear regime of each temperature *vs.* laser power density diagram. Table 3.2 and Figure 3.12 show the results. The ranges in which the heating rates have been determined are given to allow for conclusions, as the same laser powers could achieve completely different temperatures in the powder. The heating efficiency increases strongly with increasing gold concentration until a gold concentration of 3.6 mass-% and decreases from there again. Note that the heating efficiency is the increase in temperature as a function of laser power, not as a function of time. In these experiments, no temporal resolution could be achieved.

Table 3.2: Heating efficiency as a function of gold concentration. The last two columns define the laser power density as well as the temperature range in which the heating efficiency is accurate. Low and high estimates were taken from fits, where different data ranges yielded different results.

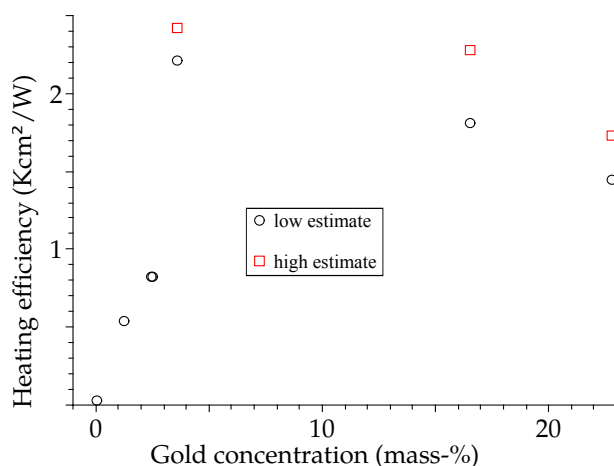| Sample/ Au conc.	Heating efficiency		Power Density range (W/cm^2)	Temperature range (K)
	low est.	high est.		
blank powder	0.036		139 - 425	311 - 322
2.5/1.2%	0.544		74 - 502	358 - 682
3.5/2.5%	0.825		122 - 454	414 - 671
5.0/2.4%	0.827		74 - 645	375 - 806
12.5/3.6%	2.217	2.426	74 - 549	481 - 1328
25/16.5%	2.284	1.815	169 - 454	1061 - 1582
37.5/22.8%	1.445	1.717	217 - 490	1092 - 1478

Figure 3.12: Heating efficiency as a function of gold concentration. Data from Table 3.2. Note that the data for the samples 3.5/2.5% and 5.0/2.4% overlaps strongly and is visible as only one data point.

The trend for lower concentrations would be expected to continue for higher concentration. Instead, for gold concentrations above 3.6 mass-% the heating efficiency seems to decrease again. The reason for this can most likely be found in the temperature ranges where it takes place. The heating efficiency for all samples started to decrease for high temperatures, as would be expected due to stronger convection and heat transfer through the support and degradation of the gold nanoparticles. In the data in Table 3.2 for the samples 25/16.5% and 37.5/22.8% it can be seen that already very low laser powers lead to significant heating of the sample above 1000 K. The decreased heating efficiency thus results from the transformation of the nanoparticles and a loss in heating efficiency already at low laser powers. One must keep in mind that the acquisition of the spectra took several minutes during which the particles were continuously illuminated. The heating efficiency could thus indeed be increasing also for higher gold concentrations.

4

CONCLUSIONS AND OUTLOOK

In this work, a more detailed study of the previously investigated system of gold nanoparticle decorated gadolinium oxide nanorods co-doped with erbium and ytterbium has been conducted. The focus laid on the radiative behaviour and morphological changes of the particles under different intensities of near infra red illumination at 980 nm.

Already the presence of a small relative amount of gold in the samples was shown to increase the heating efficiency significantly. Overall, the heating efficiency increased with the gold concentration until a certain amount. The temperature in the samples at the threshold laser power remained more or less the same, but data acquired in this work was not sufficiently reliable to derive a trend from it with certainty. As follows from increased heating efficiency and constant temperature at the threshold, the threshold laser power required to trigger black body radiation from the samples was shown to decrease strongly with increasing gold concentration. Above a certain concentration, only black body radiation was observed.

From the size determination of the gold nanoparticles, it was concluded that the temperature at the black body radiation threshold was not high enough to alter the sample morphology, which was confirmed by repeated illumination experiments and scanning transmission electron microscopy. However, if the sample is illuminated well above the threshold, significant morphology changes set in, leading to a sintering process in the oxide rods and melting the gold nanoparticles away. The change in morphology comes along with a significant increase in the black body radiation threshold, which was traced back to the loss in heating efficiency due to the gold nanoparticle melting.

While the experiments in this work have been conducted in the most reproducible conditions possible, more thought should be spent to this in the future. It has been shown that the porosity has a tremendous influence on any result that depends on the laser power density values. While the sample deposition by dispersion in acetone seems promising, more effort must be made to rule out, *e.g.*, a possible layer thickness influence and variations in the porosity due to droplet shape during deposition. As especially the samples with high gold concentrations or in general at high laser powers seem to degrade during the measurement, it might be interesting to repeat the measurements for these samples and laser powers using a spectrometre equipped with a grid and a CCD instead of a monochromator and a photomultiplier. Thereby, the spectra can be acquired much quicker (in the duration of a few milliseconds even) and the degradation process, that must be time-dependent, can be partially excluded.

If further studies are done on this topic, an interesting point to investigate might be the seemingly exponential decrease in the threshold laser power density. Here, a theoretical approach may be chosen and its results and predictions lateron compared with the experimental data in this work.

APPENDIX

A.1 LASER CALIBRATION

The laser output power was measured according to the procedure described in Section 2.2.2. Figure Figure A.1 shows the result. Fitting the linear regime slightly after the threshold current of ≈ 212 mA yielded $y = 1.493296 \cdot x - 354.8431$, where y is the laser output power at 976 nm in milliwatt and x is the laser current from the controller in mA.
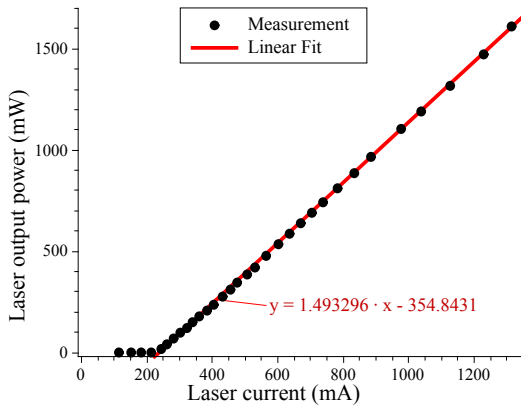

Figure A.1: Laser output power as measured and linear fit to it.

With a spot size of radius $r = 0.20$ mm, the laser power density reads

$$PD = 1.188327 \cdot x - 282.3752 \tag{A.1}$$

with x the laser current in mA and PD the laser power density in W/cm^2.

A.2 LASER POWER DENSITY ERROR AS A FUNCTION OF ANGLE AND FOCUS ERROR

When setting up the laser, focussing was always done by the eye only, leading to an error in distance from the actual focus plane. Focussing was done using an annealed powder with increased upconversion efficiency. The laser was moved until the spot appeared as round as possible. The error in the spot area was estimated to be around 30% from the mean value, leading to the same error in the laser power density.

Additionally, the laser power density on the sample varies with the angle of the sample with respect to the laser beam. Figure A.2 depicts the evolution of the laser power density as a function of the angle of the sample, where an angle of 0° means the sample is oriented parallely to the laser beam. The laser power density D is given by $D = P/A$, where P is the laser output power and A is the area that it illuminates. In the system, A is given by $A = A_0 * \sin^{-1} \phi$, where ϕ is the angle as described above. This leads to the curve in Figure A.2.

The angle of the sample usually averaged at 55° with an estimated human precision of 5°. The values of the laser power density with respect to the maximum value are shown. This leads to a variation of about 3% around the mean value.
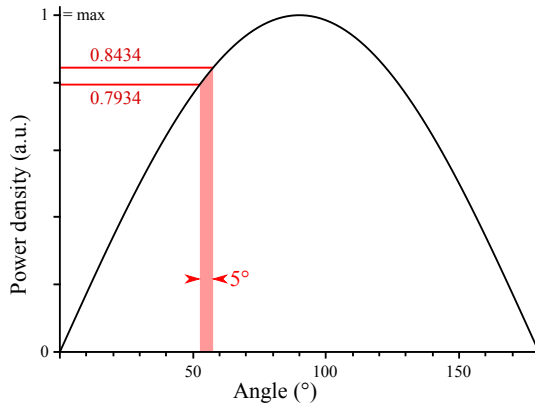

Figure A.2: Schematic of the laser power density as a function of the angle.

Both errors can add up which means that an error of 33% has to be considered for any value dependent on the laser power density in this work.

A.3   CHANGE OF SPECTRAL SHAPE WITH TEMPERATURE

Figure A.3 shows two spectra recorded for different laser power densities and therefore different local temperatures. They have been normed to the peak at 522 nm. As is obvious, the shape changes significantly. Where for low temperatures the emission from the $^4S_{3/2}$ levels makes a significant contribution, it is strongly attenuated at higher temperatures. The FIR changes from 0.781 at 411 K to 2.743 at 743 K.
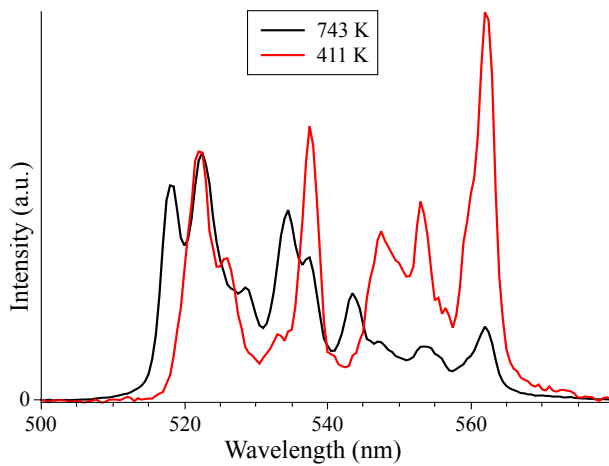

Figure A.3: Representative example of the change of the spectral shape with local temperature. The spectra are normed to the peak at 522 nm for better comparison.

BIBLIOGRAPHY

[1] G. H. Dieke, *Spectra and Energy Levels of Rare Earth Ions in Crystals* (Wiley, 1968).

[2] Wikipedia, "Seltene Erden - Bezeichnung und Einteilung," (2014).

[3] S. Barrett, "Introduction to the Rare Earths, http://www.liv.ac.uk/~sdb/research/chapter1.pdf," (2002).

[4] W. J. Miniscalco, "Optical and Electronic Properties of Rare Earth Ions in Glasses," in *Rare-Earth-Doped Fiber Lasers and Amplifiers, Revised and Expanded*, edited by M. J. F. Digonnet (CRC Press, 2001) pp. 18–130.

[5] D. Jaque and F. Vetrone, Nanoscale **4**, 4301 (2012).

[6] A. Polman, Journal of Applied Physics **82**, 1 (1997).

[7] S. Wade, S. Collins, and G. Baxter, Journal of Applied Physics **94**, 4743 (2003).

[8] M. Weber, Physical Review B **8**, 54 (1973).

[9] R. Hewes and J. Sarver, Physical Review **182**, 427 (1969).

[10] F. Song, G. Zhang, M. Shang, H. Tan, J. Yang, and F. Meng, Applied Physics Letters **79**, 1748 (2001).

[11] P. Jenouvrier, G. Boccardi, J. Fick, A.-M. Jurdyc, and M. Langlet, Journal of Luminescence **113**, 291 (2005).

[12] S. K. Singh, K. Kumar, and S. B. Rai, Sensors and Actuators A - Physical **149**, 16 (2009).

[13] B. Dong, D. P. Liu, X. J. Wang, T. Yang, S. M. Miao, and C. R. Li, Applied Physics Letters **90**, 181117 (2007).

[14] B.-C. Hwang, S. Jiang, T. Luo, J. Watson, G. Sorbello, and N. Peyghambarian, Journal of the Optical Society of America B **17**, 833 (2000).

[15] M. Hartmann, Contemporary Physics **47**, 89 (2006).

[16] P. A. Tanner, "Lanthanide luminescence in solids," in *Lanthanide Luminescence*, Springer Series on Fluorescence, Vol. 7, edited by P. Hänninen and H. Härmä (Springer, 2011) Chap. 7, pp. 184–234.

[17] J.-C. G. Bünzli and S. V. Eliseeva, "Basics of Lanthanide Photophysics," in *Lanthanide Luminescence*, Springer Series on Fluorescence, Vol. 7, edited by P. Hänninen and H. Härmä (Springer, 2011) Chap. 1, pp. 1–46.

[18] C. D. S. Brites, P. P. Lima, N. J. O. Silva, A. Millan, V. S. Amaral, F. Palacio, and L. D. Carlos, Nanoscale **4**, 4799 (2012).

[19] C. Perez-Rodriguez, L. L. Martin, S. F. Leon-Luis, I. R. Martin, K. K. Kumar, and C. K. Jayasankar, Sensors and Actuators B: Chemical **195**, 324 (2014).

[20] M. L. Debasu, D. Ananias, I. Pastoriza-Santos, L. M. Liz-Marzan, J. Rocha, and L. D. Carlos, Advanced Materials **25**, 4868 (2013).

[21] S. Redmond, S. Rand, and S. Oliveira, Applied Physics Letters **85**, 5517 (2004).

[22] C. D. S. Brites, P. P. Lima, N. J. O. Silva, A. Millan, V. S. Amaral, F. Palacio, and L. D. Carlos, Advanced Materials **22**, 4499 (2010).

[23] S. Ebert, K. Travis, B. Lincoln, and J. Guck, Optics Express **15**, 15493 (2007).

[24] V. A. Vlaskin, N. Janssen, J. van Rijssel, R. Beaulac, and D. R. Gamelin, Nano Letters **10**, 3670 (2010).

[25] M. Hartmann, G. Mahler, and O. Hess, Physical Review Letters **93**, 080402 (2004).

[26] R. Alicki and D. M. Leitner, Journal of Physical Chemistry B **119**, 9000 (2015).

[27] K. Kneipp, Y. Wang, H. Kneipp, L. T. Perelman, I. Itzkan, R. R. Dasari, and M. S. Feld, Physical Review Letters **78**, 1667 (1997).

[28] A. J. Green, *Heat Transfer from Optically Excited Gold Nanostructures into Water, Sugar, and Salt Solutions* (Ohio University, 2013) PhD thesis.

[29] J. Turkevuch, P. Stevenson, and J. Hillier, Discussions of the Faraday Society **11**, 55 (1951).

[30] H. Yuan, C. G. Khoury, H. Hwang, C. M. Wilson, G. A. Grant, and T. Vo-Dinh, Nanotechnology **23**, 075102 (2012).

[31] G. Baffou and R. Quidant, Laser & Photonics Reviews **7**, 171 (2012).

[32] P. Jain, K. Lee, I. El-Sayed, and M. El-Sayed, Journal of Physical Chemistry B **110**, 7238 (2006).

[33] A. Hohenau, A. Leitner, and F. R. Aussenegg, "Near-field and far-field properties of nanoparticle arrays," in *Surface Plasmon Nanophotonics*, Springer Series in Optical Sciences No. 131, edited by M. L. Brongersma and P. G. Kik (Springer Netherlands, 2007) p. 268, 1st ed.

[34] P. Buffat and J. Borel, Physical Review A **13**, 2287 (1976).

[35] J. Sun and S. L. Simon, Thermochimica Acta **463**, 32 (2007).

[36] G. Guenther and O. Guillon, Journal of Materials Science **49**, 7915 (2014).

[37] Y. JIA, Journal Of Solid State Chemistry **95**, 184 (1991).